Draft Manuscript for Review

Multi-stage reactive formation of troctolites in a slow-spreading oceanic lithosphere (Erro-Tobbio, Italy): a combined field and petro-chemical study.

Journal:	*Journal of Petrology*
Manuscript ID	JPET-Jun-18-0077.R3
Manuscript Type:	Original Manuscript
Date Submitted by the Author:	06-Feb-2019
Complete List of Authors:	Basch, Valentin; Università Degli Studi Di Genova, Dipartimento di Scienze della Terra, dell'Ambiente e della Vita (DISTAV) Rampone, Elisabetta; Università Degli Studi Di Genova, Dipartimento di Scienze della Terra, dell'Ambiente e della Vita (DISTAV) Crispini, Laura; Università Degli Studi Di Genova, Dipartimento di Scienze della Terra, dell'Ambiente e della Vita (DISTAV) Ferrando, Carlotta; CNRS, Géosciences Montpellier, Université de Montpellier; University of Lorraine, CRPG Ildefonse, Benoit; CNRS, Géosciences Montpellier, Université de Montpellier Godard, Marguerite; CNRS, Géosciences Montpellier, Université de Montpellier
Keyword:	Melt-rock interaction, Reactive crystallization, Crystallographic Preferred Orientation, Alpine-Apennine ophiolites, Troctolite, Mantle peridotite, Replacive formation

Multi-stage reactive formation of troctolites in a slow-spreading oceanic lithosphere (Erro-Tobbio, Italy): a combined field and petro-chemical study.

Basch, Valentin[1]; *Rampone, Elisabetta[1]; Crispini, Laura[1];

[1]DISTAV, University of Genova, Corso Europa 26, I-16132 Genova, Italy

Ferrando, Carlotta[2,3];

[2]Géosciences Montpellier, University of Montpellier, CNRS, Montpellier, France.

Current address: [3]CRPG, University of Lorraine, Nancy, France.

Ildefonse, Benoit[2]; Godard, Marguerite[2]

[2]Géosciences Montpellier, University of Montpellier, CNRS, Montpellier, France.

Corresponding Author:

Elisabetta Rampone

Dipartimento di Scienze della Terra, dell'Ambiente e della Vita (DISTAV)
Università degli Studi di Genova
Corso Europa 26
I-16132 Genova (Italy)

Email: betta@dipteris.unige.it

ABSTRACT

Many recent studies investigated the replacive formation of troctolites from mantle-related protoliths and the compositional evolution of the percolating melt during melt-rock interaction processes. However, strong structural and geochemical constraints of a replacive origin are not yet established. The Erro-Tobbio impregnated mantle peridotites are primarily associated to a hectometre-size troctolitic body and crosscutting gabbroic dikes, providing a good field control on melt-rock interaction processes and subsequent magmatic intrusions. The troctolitic body exhibits high inner complexity, with a host troctolite (*Troctolite A*) crosscut by a second generation of troctolitic metre-size pseudo-tabular bodies (*Troctolite B*). The host *Troctolite A* is characterized by two different textural types of olivine, corroded deformed millimetre- to centimetre-size olivine and fine-grained rounded undeformed olivine, both embedded in interstitial to poikilitic plagioclase and clinopyroxene. *Troctolite A* shows melt-rock reaction microstructures indicative of replacive formation after percolation and impregnation of mantle dunites by a reactive melt. The evolution of the texture and Crystallographic Preferred Orientation of olivine are correlated and depend on the melt/rock ratio involved in the impregnation process. A low melt/rock ratio allows the preservation of the protolith structure, whereas a high melt/rock ratio leads to the disaggregation of the pre-existing matrix. The mineral compositions in the *Troctolite A* define reactive trends, indicative of the buffering of the melt composition by assimilation of olivine during impregnation. The magmatic *Troctolite B* bodies are intruded within the pre-existing *Troctolite A* and are characterized by extreme textural variations of olivine, from decimetre-size dendritic to fine-grained euhedral crystals embedded in poikilitic plagioclase. This textural variability is the result of olivine assimilation during melt-rock reaction and the correlated increase in the degree of undercooling of the percolating melt. In the late gabbroic intrusions, mineral compositions are consistent with the fractional crystallization of melts modified after the reactive crystallization of *Troctolite A* and *B*. The Erro-Tobbio troctolitic body shows a multi-stage origin, marked by the transition from reactive to fractional crystallization and diffuse to focused melt percolation and intrusion, related to progressive exhumation. During the formation of the troctolitic body, the melt composition was modified and controlled by assimilation and concomitant crystallization reactions occurring at low melt supply. Similar processes were described in ultraslow-spreading oceanic settings characterized by scarse magmatic activity.

Keywords: Alpine-Apennine ophiolites; Melt-rock interaction; Reactive crystallization; Replacive formation; Crystallographic Preferred Orientation.

1. INTRODUCTION

Recent studies demonstrated that melt-rock interactions can lead to extensive small-scale structural and geochemical heterogeneities within the percolated mantle peridotites at different depths (e.g., Quick, 1981, 1982; Dijkstra *et al.*, 2002, 2003; Lissenberg & Dick, 2008; Soustelle *et al.*, 2009, 2010, 2014; Collier & Kelemen, 2010; Higgie & Tommasi, 2012, 2014; Tursack & Liang, 2012; Saper & Liang, 2014; Dygert *et al.*, 2016; Paquet *et al.*, 2016; Renna *et al.*, 2016; Sanfilippo *et al.*, 2017), and can act as a rock-forming process for replacive lithotypes. In extensional settings worldwide, spinel harzburgites and spinel dunites showing decoupled bulk and mineral chemistry features have been interpreted as the replacive product of open-system reactive melt percolation at spinel-facies depth, driven by pyroxene dissolution and olivine crystallization (e.g., Takazawa *et al.*, 1992; Godard *et al.*, 1995; Kelemen *et al.*, 1995a, b, 2000, 2007; Dick *et al.*, 2008, 2010; Piccardo *et al.*, 2007; Rampone *et al.*, 2004; 2008; Rampone & Borghini, 2008; Lambart *et al.*, 2009; Liang *et al.*, 2011; Pirard *et al.*, 2013; Dygert *et al.*, 2016). On the other hand, plagioclase-rich peridotites have been ubiquitously found in ophiolitic and oceanic settings and interpreted as the replacive product of melt impregnation that occurred at shallower plagioclase facies conditions, leading to olivine dissolution and interstitial plagioclase and pyroxene crystallization (e.g., Van der Wal & Bodinier, 1996; Garrido & Bodinier, 1999; Dijkstra *et al.*, 2002, 2003; Borghini *et al.*, 2007; Rampone & Borghini, 2008; Tursack & Liang, 2012; Saper & Liang, 2014; Basch *et al.*, 2018).

Melt-rock interactions have also been increasingly invoked in the formation of the oceanic crust and described as a geochemical key process in the compositional evolution of the percolating MORB melts from several lines of evidence: (1) dissolution-precipitation microstructures and geochemical zoning in lower crustal gabbros (Lissenberg & Dick, 2008; Lissenberg *et al.*, 2013; Lissenberg & MacLeod, 2016), (2) the composition of melt inclusions in lava phenocrysts (Laubier *et al.*, 2014; Coumans *et al.*, 2016), (3) peculiarities in the compositional variations of mid-ocean ridge basalts (MORBs), not consistent with a process of fractional crystallization alone (Collier & Kelemen, 2010; Van den Bleeken *et al.*, 2011; Paquet *et al.*, 2016; Sanfilippo *et al.*, 2016a), (4) the structural and geochemical mantle inheritance inferred in olivine-rich troctolites enclosed in the lowermost oceanic crust. These olivine-rich gabbroic rocks are thought to represent the replacive product of the interaction between a dunitic matrix and a percolating tholeiitic melt in disequilibrium with its host rock (Lissenberg & Dick, 2008; Suhr *et al.*, 2008; Drouin *et al.*, 2009, 2010; Renna & Tribuzio, 2011; Higgie & Tommasi, 2012; Sanfilippo & Tribuzio, 2012; Sanfilippo *et al.*, 2013, 2014, 2015a, 2016b; Rampone *et al.*, 2016; Basch, 2018; Basch *et al.*, 2018; Ferrando *et al.*, 2018). However, during the dissolution-precipitation reaction, the texture of the olivine matrix progressively evolves towards a cumulate-like poikilitic texture of the olivine-rich gabbroic rock (Suhr *et al.*, 2008; Drouin *et al.*, 2010; Basch *et al.*, 2018), thus calling for the need of strong structural and geochemical constraints to discriminate between a magmatic and a replacive origin of the lithotype.

Previous studies have documented that the Alpine-Apennine ophiolitic peridotites record various stages of melt-rock interaction occurring at different mantle depths (e.g. Rampone & Borghini, 2008; Piccardo & Guarnieri, 2010; Rampone *et al.*, 2018). In the Erro-Tobbio ultramafic unit (Voltri Massif, Ligurian Alps), peridotites preserve microstructures and geochemical compositions indicative of a multi-stage melt-rock interaction history, related to progressive exhumation of this mantle sector from spinel facies depths to shallow oceanic environments (Rampone *et al.*, 2004, 2005, 2016; Borghini & Rampone, 2007; Borghini *et al.*, 2007; Piccardo & Vissers, 2007; Rampone & Borghini, 2008). In places, impregnated plagioclase peridotites are found in irregular contact with a hectometre-size troctolitic body, later crosscut by troctolitic and gabbroic dykes. Previous studies inferred a prevalent magmatic origin for these gabbroic rocks (Borghini & Rampone, 2007; Borghini *et al.*, 2007; Rampone & Borghini, 2008). In a recent study on the geochemistry of olivine, Rampone *et al.* (2016) highlighted the important role of melt-rock interaction in the origin of olivine-rich troctolites. The Erro-Tobbio peridotite-gabbro association thus appears an ideal case study to track the structural and geochemical changes in mantle peridotites progressively transforming to replacive troctolites during reactive dissolution (i.e. a dissolution-precipitation process; Liang, 2003), and to identify the role of reactive versus fractional crystallization in the origin of olivine-bearing gabbroic rocks. In this study, we present a detailed field mapping of the internal structural complexity of the troctolitic body, coupled with Electron Backscatter Diffraction (EBSD) measurements, and mineral major elements analyses (by Electron Probe Micro-Analyser) of the host spinel and plagioclase peridotite, the troctolitic body, and the gabbroic intrusions.

Major outcomes of this work are: (1) the documented correlation between the textural evolution of the olivine matrix and the modification of the olivine Crystallographic Preferred Orientation (CPO) during replacive formation of the olivine-rich troctolite, and (2) the demonstrated modification of the melt composition during the melt-rock interaction history, leading to peculiar mineral compositional trends in the gabbroic intrusions, shifted towards Mg-rich olivines and clinopyroxenes.

2. STRUCTURAL AND PETROLOGIC BACKGROUND

The Alpine-Apennine ophiolites are predominantly constituted by mantle peridotites and represent lithospheric analogues of ocean/continent transition zones and slow- to ultra-slow spreading environments (Rampone *et al.*, 1997, 2004, 2008; Rampone & Piccardo, 2000; Müntener & Piccardo, 2003; Müntener *et al.*, 2004; Piccardo *et al.*, 2004; Borghini *et al.*, 2007; Manatschal & Müntener, 2009). They are thought to represent the lithospheric remnants of the narrow Jurassic Ligurian Tethys oceanic basin, opened by passive lithosphere extension and breakup of the continental lithosphere, leading to slow-spreading oceanization (Rampone & Piccardo, 2000; Manatschal & Müntener, 2009).

The Erro-Tobbio ultramafic body (Voltri Massif, Ligurian Alps, Fig. 1) exposes kilometre-scale unaltered peridotites, mostly devoid of Alpine overprint (Bezzi & Piccardo, 1971; Chiesa *et al.*, 1975; Ernst & Piccardo, 1979; Ottonello *et al.*, 1979; Hoogerduijn Strating *et al.*, 1990, 1993; Piccardo *et al.*, 1990, 1992, 2004; Scambelluri *et al.*, 1991; Vissers *et al.*, 1991; Borsi *et al.*, 1996; Capponi *et al.*, 1999; Rampone *et al.*, 2004, 2005), allowing the study of the pre-Alpine structural and chemical mantle evolution. The Erro-Tobbio unit is mostly made of variably serpentinized spinel-bearing lherzolites to harzburgites. Previous petrologic and structural studies documented a tectono-metamorphic decompressional evolution of these mantle rocks, from deep lithospheric settings (P > 15-20 kbar) to shallow depths (P < 5 kbar), with a progressive reequilibration from spinel- to plagioclase- to amphibole-facies conditions (Hoogerduijn Strating *et al.*, 1990, 1993; Vissers *et al.*, 1991; Rampone *et al.*, 2005), and the development of extensional shear zones forming spinel tectonites, plagioclase-, hornblende-, chlorite-bearing mylonites and serpentinite mylonites (Hoogerduijn Strating *et al.*, 1993). This extension-related exhumation was accompanied by multiple episodes of melt percolation and intrusion, namely: 1) a first open-system olivine-saturated reactive porous flow at spinel-facies conditions, leading to the dissolution of mantle clinopyroxene and orthopyroxene, and crystallization of olivine; 2) a melt-rock reaction at plagioclase-facies conditions (< 8-10 kbar) leading to the formation of plagioclase-bearing impregnated peridotites, by dissolution of olivine and crystallization of plagioclase ± opx ± cpx; 3) multiple episodes of gabbroic intrusions at shallow depths (P < 5kbar) (Piccardo *et al.*, 2004; Rampone *et al.*, 2004, 2005, 2014, 2016, 2018; Borghini *et al.*, 2007; Borghini & Rampone, 2007; Piccardo & Vissers, 2007; Rampone & Borghini, 2008). Geochronological studies on gabbroic rocks from the Alpine-Apennine ophiolites indicate a large time span of gabbroic intrusions (~20 Ma) in the Alpine Tethys (Rampone *et al.*, 2014 and reference therein). The Erro-Tobbio gabbroic intrusions yield the oldest Sm-Nd age of the crustal gabbroic sequences within the Alpine-Apennine ophiolites with an age of 178 ± 5 Ma (Rampone *et al.*, 2014), therefore representing early melt intrusions in thinned lithospheric mantle exhumed at ocean-continent transition domains (Rampone & Piccardo, 2000; Manatschal & Müntener, 2009).

In the South-Eastern part of the Erro-Tobbio peridotite, the impregnated mantle peridotites are in irregular contact with a hectometre-size troctolitic body, previously described as a *primitive cumulate body* (Fig. 1; Borghini & Rampone, 2008; Borghini *et al.*, 2007; Rampone & Borghini, 2008; Rampone *et al.*, 2016). Gabbroic dykes crosscut all mantle structures, as well as the troctolitic body-impregnated peridotite contact (Borghini *et al.*, 2007). Rampone *et al.* (2016) recently demonstrated the important effect of the olivine-dissolving, plagioclase-crystallizing melt-rock interaction in the Erro-Tobbio troctolitic body mineral compositions. It leads to significant enrichments in specific trace elements (Zr, Hf, Ti, HREE), coupled with strong HFSE/REE fractionation in olivine.

Previous geochemical studies documented a significant change in the melt composition between the impregnation event observed in the plagioclase peridotites (Rampone *et al.*, 2005), and the late troctolite-gabbro intrusions. Impregnating melts had an orthopyroxene-saturated LREE-depleted signature, consistent with single depleted melt increments produced by near-fractional melting of a MORB-type asthenospheric mantle source (Piccardo *et al.*, 2004; Borghini *et al.*, 2007; Rampone & Borghini, 2008). A similar origin has been inferred for other Alpine-Apennine impregnated peridotites (e.g. Rampone *et al.*, 1997, 2008, 2018; Piccardo *et al.*, 2007). On the other hand, parental melts to the troctolitic body and late gabbroic discrete intrusions resemble N-MORB-type aggregated melts (Rampone *et al.*, 1998, 2014, 2016; Borghini & Rampone, 2007; Borghini *et al.*, 2007; Rampone & Borghini, 2008). Based on available time constraints on the extensional evolution of the Erro-Tobbio mantle, i.e. the Permian age of plagioclase-facies recrystallization documented in impregnated peridotite mylonites (Rampone *et al.*, 2005), and the Jurassic age of gabbroic intrusions (Rampone *et al.*, 2014), melt impregnation in the plagioclase peridotites and subsequent troctolite-gabbro intrusion events were likely uncorrelated.

3. FIELD RELATIONSHIPS

The investigated area exposes a 500-metre wide ultramafic body surrounded by serpentinized high-pressure, low-temperature Alpine shear zones. The ultramafic body preserves a pre-Alpine mantle history, displaying the association between mantle peridotites and ultramafic-mafic bodies and intrusions (from plagioclase wehrlites to troctolites to olivine gabbros) (Fig. 1; Borghini & Rampone, 2007; Borghini *et al.*, 2007; Rampone & Borghini, 2008; Rampone *et al.*, 2016). Mantle peridotites are ***Plagioclase-bearing lherzolites*** showing in places a weak tectonic foliation defined by ortho- and clinopyroxene shape-preferred orientations. They are primarily associated to metre-size dunitic pods and centimetre-size pyroxenite layers showing a constant NNE-SSW orientation and strongly dipping to the East (Fig. 1). In the northernmost part of the ultramafic body, the plagioclase lherzolites are in irregular contact with a hectometre-size troctolitic body. The contact is marked by the occurrence of troctolitic and plagioclase-bearing wehrlite apophyses into the mantle peridotites, crosscutting the pyroxenite banding (Borghini & Rampone, 2007; Borghini *et al.*, 2007; Rampone & Borghini, 2008; Rampone *et al.*, 2016). Detailed mapping and sampling in selected outcrops revealed that the inner troctolitic body is characterized by a high modal compositional variability, from plagioclase wehrlite to troctolite to dunite, and a structural complexity characterized by different generations of troctolites showing crosscutting relationships and highly variable olivine texture. In the following, based on these structural criteria, we distinguish different types of troctolites within the mafic body.

Troctolite A is in irregular contact with the mantle peridotites through a transition zone (Fig. 1) characterized by *plagioclase lherzolites* with decimetre-thick crosscutting troctolite and plagioclase-bearing wehrlite apophyses (Fig. 2a) in which it is difficult to easily distinguish the different lithologies (Fig. 1). *Troctolites A* show variable olivine modal contents (from 55 to 74 vol%; Table 1, Fig. 2b,c) and interstitial plagioclase ± clinopyroxene, and it includes decimetre-size dunitic pods (Fig. 2d). The modal composition variability between olivine-rich and plagioclase-rich troctolite forms a local sub-vertical decimetre-size layering showing a NNW-SSW orientation, dipping to the East (Figs. 1, 2b).

Troctolite B is found as decimetre- to metre-size pseudo-tabular elongated bodies crosscutting the layering of plagioclase enrichment in *Troctolite A* (Figs. 2c, 3a), and showing irregular to sharp contacts with the host troctolite (Figs. 2c, 3a,b). *Troctolite B* bodies display extreme olivine textural variations at the scale of a few centimetres, from millimetre-size euhedral olivine crystals to centimetre- and decimetre-size hopper and dendritic olivine crystals (Fig. 3c,d,e). The olivine textural layering observed in *Troctolite B*, between granular and dendritic portions of the pseudo-tabular bodies (Fig. 3e) shows NNE-SSW strike and dips steeply to the East, similarly to the plagioclase enrichment layering in *Troctolite A* (Fig. 1).

The peridotites and troctolitic bodies are both intruded by decametre-size ***Gabbroic intrusions***, centimetre- to metre-thick troctolitic to olivine gabbro dykes and centimetre-thick dykelets, all stiking NNW-SSE, and dipping to the East (40-50°; Figs. 1, 2a; Borghini & Rampone, 2007; Borghini *et al.*, 2007) although in places dykelets occur as conjugate pairs. Dykes and dykelets are in straight and sharp contact with the host rock and show no chilled margins. They display a grain-size variability, from fine grains towards the margin of the intrusion (millimetre-size crystals), to coarse grains (centimetre-size crystals) in the core of the dyke. Figure 4 summarizes the field relationships mapped in the studied Erro-Tobbio ultramafic body, between *Plagioclase lherzolites*, *Troctolite A*, *Troctolite B*, and *Gabbroic Intrusions*.

4. SAMPLING AND ANALYTICAL METHODS

We used samples of *Spinel Lherzolites*, *Plagioclase Lherzolites*, *Troctolites* and *Gabbroic intrusions* collected during previous petrological investigations of the studied area (Fig. 1; Rampone *et al.*, 2004, 2005, 2014, 2016; Borghini & Rampone, 2007; Borghini *et al.*, 2007), as well as newly collected samples of *Troctolite* and *Gabbroic intrusions*. The *Spinel* and *Plagioclase Lherzolites* have been sampled in a location nearby the troctolitic body, where the alteration is much less developed than elsewhere within the Erro-Tobbio peridotites. These samples are used as a structural and chemical reference of the mantle protolith, prior to the formation of the troctolitic body and gabbroic dykes. Table 1 reports the modal composition of the 40 studied samples, namely 3 spinel lherzolites, 4 plagioclase lherzolites, 11 troctolites A, 1 dunite pod, 5 wehrlite and troctolite apophyses, 10 troctolite B, and 6 troctolitic to olivine gabbro intrusions. We performed structural EBSD mapping of all samples, and mineral major (EPMA) element chemical analyses of 24 samples, namely 2 spinel lherzolites, 2 plagioclase lherzolites, 7 troctolites A, 1 dunite pod, 2 wehrlite and troctolite apophyses, 5 troctolites B, and 5 troctolitic to olivine gabbro intrusions. Detailed methodologies for EBSD and mineral major elements analyses can be found in Supplementary Material.

5. PETROGRAPHY

Spinel lherzolites show protogranular to porphyroclastic assemblages of olivine, orthopyroxene, clinopyroxene and spinel grains. Olivine and pyroxenes (orthopyroxene + clinopyroxene) are deformed, and display kink bands and undulatory extinctions, respectively. Clinopyroxenes and orthopyroxenes both show thin exsolution lamellaes of the complementary pyroxene. Spinels are found as granular grains in the lherzolitic matrix and in orthopyroxene + spinel symplectites at the rim of orthopyroxene porphyroclasts, previously described as an effect of cooling of the peridotites and equilibration at lithospheric temperatures (970-1100°C; Rampone *et al.*, 2005; Rampone & Borghini, 2008). The spinel lherzolites display melt-rock interaction microstructures with the development of olivine embayments replacing mantle pyroxenes (i.e. pyroxene dissolution and olivine crystallization). These microstructures, associated to an increase of olivine modal compositions, have been extensively described in the Alpine-Apennine ophiolites (Piccardo *et al.*, 2004; Rampone *et al.*, 2005, 2008; Piccardo & Vissers, 2007; Rampone & Borghini, 2008; Basch *et al.*, 2018) and in the Othris Massif (Dijkstra *et al.*, 2003), and were interpreted as the result of a pyroxene-dissolving, olivine crystallizing reactive melt percolation at spinel facies.

Plagioclase lherzolites have been previously described as the replacive product of melt impregnation of the spinel lherzolites (Borghini *et al.*, 2007). They show similar textures and microstructures to the spinel facies protolith but are characterized by an enrichment in undeformed interstitial plagioclase and orthopyroxene (Table 1), developing embayments on kinked olivine and exsolved clinopyroxene. These melt-rock reaction microstructures are indicative of an orthopyroxene-saturated composition of the impregnated melt, as previously described in the Alpine-Apennine ophiolitic peridotites (Rampone *et al.*, 1997, 2005, 2008, 2016, 2018; Müntener & Piccardo, 2003; Piccardo *et al.*, 2004; Borghini & Rampone, 2007; Borghini *et al.*, 2007; Rampone & Borghini, 2008; Basch *et al.*, 2018) and in the Othris Massif (Dijkstra *et al.*, 2003).

Troctolite A shows a hypidiomorphic texture and variable grain size, from centimetre-size anhedral to millimetre-size euhedral olivine crystals. Olivine occurs either i) as fine-grained undeformed euhedral crystals embedded in interstitial to poikilitic plagioclase and clinopyroxene (Fig. 5a,b), or ii) as coarse (up to centimetre-size) deformed corroded grains, displaying kink bands (Fig. 5c,d). These two types of olivine are commonly found together, and in places fine-grained euhedral crystals of olivine embedded in poikilitic plagioclase or clinopyroxene show the same crystallographic orientation as a neighbouring coarsed corroded grain of olivine (Fig. 5c).

Within *Troctolite A*, the textural variability includes small dunitic domains (olivine > 90 vol%; Fig. 6a,b,c), in which interstitial plagioclase surrounds millimetre-size to centimetre-size zones free of interstitial minerals, and plagioclase-rich domains (Fig. 6d), in which single olivines are entirely embedded in poikilitic plagioclase ± clinopyroxene. Clinopyroxene, orthopyroxene, and amphibole are found as thin "vermicular" crystals at the contact between olivine and poikilitic minerals and have been previously interpreted as post-cumulus crystallization of trapped melts (progressively evolving during late-stage closed system crystallization; Borghini & Rampone, 2007; Borghini *et al.*, 2007). Spinels are found in the matrix both associated to olivine as millimetre-size corroded grains (Fig. 6a,d), and associated to poikilitic plagioclase and clinopyroxene, as subhedral to euhedral smaller grains (~100-200 µm, Fig. 6d). ***Troctolite apophyses*** (part of *Troctolite A*) are very rich in coarse deformed corroded grains of olivine (Fig. 6b), and undeformed fine-grained olivine is rare.

Troctolite B pseudotabular bodies crosscut the host *Troctolite A* structures. They are characterized by lower olivine modal contents (from 45 to 60 vol%**,** Table 1) than the host

Troctolite A (from 55 vol% to 97 vol% olivine; Table 1). Moreover, *Troctolite B* shows an extreme olivine textural variation, from millimetre-size euhedral crystals (Fig. 7a) to centimetre-size hopper (Fig. 7b), to decimetre-size dendritic and skeletal olivine (Figs. 3b,c,d,e, 7c,d), all showing absent to weak deformation (Fig. 6e). In places, this textural variability leads to the formation of a layering (Fig. 4), but all olivine morphologies can also be found together at the centimetre-scale (Fig. 6e).

The ***Gabbroic intrusions*** (gabbroic lenses, dykes and dykelets) are mostly made of olivine gabbros and minor troctolites, displaying hypidiomorphic texture and fine- to coarse-grained olivine size. Subhedral plagioclase is the main rock-forming mineral (from 59 to 69 vol% modal content of plagioclase, Table 1). Clinopyroxene is mostly found as large anhedral crystals including pre-existing euhedral plagioclase ± olivine. Olivines (from 15 to 30 vol% modal olivine, Table 1) are found both as euhedral grains included in plagioclase ± clinopyroxene, and anhedral interstitial crystals in plagioclase-clinopyroxene-olivine aggregates, indicative of a eutectic crystallization of the melt. These textural features in the gabbroic intrusions are indicative of an olivine – plagioclase – clinopyroxene crystallization sequence.

6. OLIVINE CRYSTALLOGRAPHIC PREFERRED ORIENTATIONS

In all studied samples of *Spinel lherzolite*, *Plagioclase Lherzolites* and *Troctolite*, a clear and representative olivine CPO could be quantified, however because of large grain size of plagioclase and pyroxenes (Fig. 8; Bunge, 1982; Ben Ismail & Mainprice, 1998), no reliable CPO of the interstitial minerals could be obtained at the thin section scale. In *Gabbroic intrusions*, fine-grained euhedral plagioclase crystals also allow a representative quantification of the plagioclase CPO (Fig. 9).

Olivines in ***Spinel Lherzolites*** (ETR2, ETR4A, ETR4B in Table 1) are characterized by an axial-[100] CPO, with [100] axis showing the strongest preferred orientation in the foliation plane, parallel to the lineation, [010] axis maximum oriented normal to the foliation plane, and [001] maximum within the foliation plane, normal to the lineation (Fig. 8). The J-Index, representative of the fabric strength (e.g., Bunge, 1982; Ben Ismail & Mainprice, 1998; Mainprice *et al.*, 2014), ranges from 3.64 to 5.59 in spinel peridotites. Most natural peridotites show J-Index values of olivine CPO between 2 and 20 (Tommasi *et al.*, 2000; Soustelle *et al.*, 2009).

Olivines in ***Plagioclase Lherzolites*** (P1A, P1B in Table 1) are characterized by a strong axial-[010] CPO (J-Index = 5.5-7), with the strongest axis orientation being [010] normal to the foliation, and a girdle orientation of [100] and [001] within the foliation plane, showing a maximum parallel and normal to the lineation, respectively (Fig. 8).

In ***Troctolite A with dunitic aggregates*** (Fig. 6a,b,c; MF7A1, MF7A2, MF7C1, MF96A, MF96B in Table 1) and in the *Dunite* pod associated to the *Troctolite A* (MF104A in Table 1, Fig. 2c), all samples are characterized by a relatively weak (J-Index = 2.04-3.83) but clear axial-[100] olivine CPO, with strongly oriented [100] axes within the foliation plane, [010] axes normal to the foliation, and a scatter of the [001] olivine axis orientation (Fig. 8). This olivine CPO is similar to that observed in the *Spinel Lherzolites* (Fig. 8). *Troctolite Apophyses* show a range of weak olivine CPOs from axial-[100] to axial-[010] (J-Index = 1.86-2.1), similar to the CPO observed in *Spinel Lherzolites* and *Plagioclase Lherzolites*, respectively.

Troctolite A without dunitic aggregates (Fig. 6d; MF21, MF15, MF97, MF102B1 in Table 1) shows a very weak to random orientation of the [100] and [010] axes, and increased concentrations of the [001] olivine axis (J-Index = 2.17-3.06).

Gabbroic intrusions (MF20II, MF24, MF11A1, MF99 in Table 1) show very weak olivine CPO (J-Index = 1.21-1.83) characterized by [010] and [001] showing clear maxima normal and within the foliation plane, respectively (Fig. 9). Plagioclase shows a weak (J-Index = 1.79-4.60) (010)[100] CPO characterized by a strong orientation of the [010] axis normal to the foliation plane (Fig. 9).

Olivines in the granular part of ***Troctolite B*** (MF46A, MF94B in Table 1) are characterized by a strong orientation of the [010] and [001] axes normal and within the foliation plane, parallel to the lineation, respectively (Fig. 9). This (010)[001] olivine CPO is similar to that observed in the *Gabbroic intrusions* (Benn & Allard, 1989, Jousselin *et al.*, 2012). The coarse poikilitic minerals in Troctolite B samples do not allow a reliable characterization of the Plagioclase CPO at the thin section scale (Fig. 9).

7. MAJOR ELEMENT MINERAL COMPOSITIONS

Representative major element compositions of olivine, clinopyroxene, plagioclase, orthopyroxene and spinel analyzed in *Spinel lherzolites, Plagioclase lherzolites, Troctolites A, Dunite, Troctolites B* and *Gabbroic intrusions* are reported in Tables 2-6 and the complete dataset is given in Supplementary Tables S1-5. Overall our data show consistency with mineral compositions reported in previous studies of the Erro-Tobbio peridotites and associated gabbroic rocks (troctolitic body and gabbroic lenses and dykes) (Rampone *et al.*, 1993, 1998, 2004, 2005, 2016; Borghini & Rampone, 2007; Borghini *et al.*, 2007).

Olivines in *Spinel lherzolites* and *Plagioclase lherzolites* show rather homogeneous high Forsterite contents (Fo = 89.5-90.5 mol% and Fo = 89.6-90.3 mol%, respectively; Fig. 10a) (Table

2). Olivines in *Troctolites A* and *B* have lower and more variable Forsterite contents (Fo = 87.3-89.2 mol%). Within the troctolitic body, the main variations are observed between samples rather than within a single sample (Fig. 10a). No correlation is observed between the different olivine morphologies described in *Troctolite A* or *B* and Forsterite contents. Olivines within the *Dunite* pod associated to *Troctolite A* show contents of Forsterite = 88.2-89.1 mol% similar to olivines in the *Troctolite A* (Fig. 10a). The *Wehrlite Apophysis* MF47A (Table 1) has the lowest Forsterite content analyzed in *Troctolite A* (Fo = 87.3-87.7 mol%). *Gabbroic intrusions* show a wide range of variation of Forsterite contents in olivine from primitive compositions in the troctolitic intrusions (up to Fo = 89.2 mol%) to more evolved compositions in olivine gabbros (Fo = 81.3 mol%) (Table 1; Fig. 10b).

Clinopyroxene cores in *Spinel Lherzolites* show high Mg-numbers (Mg# = 90.0-91.6 mol%), high Cr_2O_3 = 0.82-1.33 wt% and Al_2O_3 = 5.2-7.4 wt%, and low TiO_2 = 0.30-0.58 wt% (Table 3; Fig. 11a,b) contents. Impregnated *Plagioclase Lherzolites* show similar Mg-value (Mg# = 89.6-91.1 mol%) and TiO_2 = 0.4-0.53 wt% contents, higher Cr_2O_3 = 1.02-1.40 wt%, and lower Al_2O_3 = 2.83-5.27 wt% concentrations. *Gabbroic intrusions* exhibit clinopyroxene compositions consistent with olivine gabbros and troctolites from the South-West Indian Ridge (Dick *et al.*, 2002), with a positive correlation between Mg-number (Mg# = 83.5-90.8 mol%), Cr (Cr_2O_3 = 0.18-1.15 wt%), and Al (Al_2O_3 = 2.4-3.7 wt%), and negative correlation with Ti (TiO_2 = 0.42-1.41 wt%) (Fig. 11a,b). Clinopyroxenes in *Troctolite A* (and associated *Dunite*) and *Troctolite B* show high Cr (Cr_2O_3 = 1.17-1.67 wt%) and low Al (Al_2O_3 = 3.1-5.0 wt%) and Ti contents (TiO_2 = 0.12-0.92 wt%) (Fig. 11a,b).

Figure 11c,d shows the correlation between the clinopyroxene composition and its microstructural site. As previously documented by Borghini & Rampone (2007), clinopyroxenes in *Troctolite A* show progressively decreasing Cr_2O_3 (Cr_2O_3 = 0.78-1.67 wt%) and increasing TiO_2 (TiO_2 = 0.12-1.24 wt%) contents from core to rim to interstitial to vermicular microstructural sites, at constant Mg-number (Mg# = 87.7-91.0 mol%).

The Cr_2O_3, Al_2O_3 and TiO_2 compositional variability in clinopyroxene is well observed in major elements core-rim profiles within single clinopyroxene grains (Fig. 12a-d). A progressive decrease in Cr_2O_3 (from 1.5 to 1.0 wt%) and Al_2O_3 (from 4 to 3 wt%), coupled with an increase in TiO_2 (from 0.4 to 1 wt%) is observed in the profiles, from the inner core towards the contact between clinopyroxene and olivine (Rampone *et al.*, 2005). As documented by Borghini *et al.* (2007), the strong heterogeneity of Cr_2O_3, TiO_2 and Al_2O_3 in clinopyroxenes of *Troctolites A* (Fig. 11c,d) is thus related to within-sample variations clearly correlated with microstructural site.

Geochemical variations in the profiles are observed from ~200µm to the contact with the olivine (Fig. 12a-d).

Plagioclases in the *Troctolite A* (Table 4) are characterized by low and variable Anorthite contents (An = 52.9-66.8 mol%) (Fig. 13). The same variability is observed in *Troctolites B*, with Anorthite contents = 55.1-66.1 mol%. Plagioclases in *Gabbroic intrusions* show lower Anorthite = 51.6-62.7 mol%. In all samples of *Troctolite A* and *Troctolite B*, a correlation is observed between the microstructural site and the Anorthite content of the analyzed plagioclase crystal. Thin interstitial crystals and rims of large grains systematically show lower Anorthite than the plagioclase cores (Fig. 13), leading to a variation of Anorthite content up to 10 mol% within a single sample, in both *Troctolites A* and *Troctolites B*.

Again, these geochemical variations are well observed in major element profiles from core to rim of plagioclase crystals, at the contact with olivine. A progressive decrease in Anorthite content (from 66 to 56 mol%), CaO (from 14 to 12 wt%), and Al_2O_3 (from 31 to 30 wt%) is observed in the profiles towards the rim and the contact with olivine (Fig. 12e-h), as previously documented by Borghini & Rampone (2007). Therefore, as observed for clinopyroxene, the strong compositional variation reported in single samples of *Troctolite A* and *B* (up to 10% Anorthite content, Fig. 3.13) is not due to variations between different crystals but to the zonation observed at the scale of a single grain (Fig. 12e-h). As documented in the clinopyroxene-olivine profiles, the chemical zoning in plagioclase is observed from ~200µm to the contact with the olivine, irrespective of its textural type (coarse deformed corroded grain or small undeformed granular crystal.

In *Gabbroic intrusions*, no systematic zoning is observed in plagioclase, and the analyzed range of Anorthite concentration is mainly observed between samples (Fig. 13), with plagioclase in troctolitic dykes showing higher Anorthite contents (MF11A1, MF99, An = 53.8-62.7 mol%; Table 1) than plagioclases forming the olivine gabbro dykes (MF2A, MF24, An = 51.6-54.6 mol%; Table 1).

Orthopyroxenes (Table 5) analyzed in evolved *Gabbroic intrusions* show lower Mg-number (Mg# = 84.53 mol%) than the homogeneous orthopyroxene compositions analyzed in *Spinel* and *Plagioclase Lherzolites* (Mg# = 89.64-90.54 mol%).

Spinels in *Spinel Lherzolites* (Table 6) exhibit high Mg-number (Mg# = 66.9-72.8 mol%), low Cr-number (Cr# = 14.2-18.6 mol%), and very low TiO_2 (0.02-0.16 wt%), similar to spinel compositions in plagioclase-free peridotites from the South-West Indian Ridge (Seyler *et al.*, 2003). In *Gabbroic intrusions*, spinels show low Mg-number (Mg# = 25.2-36.1 mol%), and high Cr-number (Cr# = 63.6-69.0 mol%) and TiO_2 (1.22-1.49 wt%).

In *Troctolites A, Dunites* and *Troctolites B*, spinels show Mg-numbers (Mg# = 19.2-55.6 mol%) and Cr-numbers (Cr# = 40.5-64.5 mol%) intermediate between spinel compositions in the *Spinel lherzolites* and the *Gabbroic intrusions*, and a negative correlation is observed between the Mg-number and the Cr-number, consistent with spinel compositions in Troctolites from the Mid-Atlantic Ridge (Miller *et al.*, 2009). Some spinels in *Troctolites A*, *Troctolites B*, and most of them in *Dunites* show strong enrichments in TiO_2 (0.79-3.27 wt%), up to twice the TiO_2 concentrations analyzed in *Gabbroic intrusions*. The negative correlation between Mg-number and TiO_2 concentrations in spinel analyzed in *Troctolites A*, associated *Dunites* and *Troctolites B* is consistent with the trend reported for spinels analyzed in troctolites from the Mid-Atlantic Ridge (Miller *et al.*, 2009).

Figure 14a shows the Mg-Fe partitioning between olivine and clinopyroxene in all studied lithotypes. Overall, the studied samples show a positive correlation between Forsterite contents in olivine (from Fo = 81.3 mol% in *Gabbroic intrusions* to Fo = 90.5 mol% in *Spinel Lherzolite*) and Mg-value in clinopyroxene (from Mg# = 83.5 mol% in *Gabbroic intrusions* to Mg# = 91.6 mol% in *Spinel Lherzolite*). This correlation is consistent with the Mg-Fe equilibrium lines calculated between olivine and clinopyroxene by Lissenberg & Dick (2008) ($Kd_{ol/cpx}$ (Fe#) = 1.30) (Fig. 14a). Couples of olivine and clinopyroxene cores in *Troctolites A*, *Dunite*, and *Troctolites B* show compositions (Fo = 87.3-89.2 mol%, Mg# = 87.7-91 mol%) that are intermediate between the Mg-rich couples analyzed in *Spinel* and *Plagioclase Lherzolites* (Fo = 89.5-90.5 mol%, Mg# = 89.6-91.6 mol%) and the most evolved compositions in *Gabbroic intrusions* (Fo = 81.3-89.2 mol%, Mg# = 83.5-90.8 mol%).

Figure 14b shows Anorthite and Forsterite contents (mol%) in plagioclase-olivine core couples in *Troctolite A*, *Troctolite B* and *Gabbroic intrusions*. Within the troctolitic body, plagioclase-olivine couples show significant variations in Anorthite content of plagioclase cores (An = 58.4-66.8 mol%) at constant Forsterite composition in associated olivines (87.3-89.2 mol%), similar to what was reported at the easternmost South-West Indian Ridge (61-67°E) (Paquet *et al.*, 2016). By contrast, *Gabbroic intrusions* define a trend of evolution characterized by a positive correlation between Anorthite content in plagioclase cores and Forsterite content in olivine (from $An_{51.6}$-$Fo_{81.3}$ to $An_{62.7}$-$Fo_{89.2}$). This trend in *Gabbroic intrusions* shows a similar slope to the compositional arrays defined by olivine gabbros in the oceanic lower crust from the South-West Indian Ridge (Hole 735B: Dick *et al.*, 2002), Mid-Atlantic Ridge (Ross & Elthon, 1997; Lissenberg & Dick, 2008; Suhr *et al.*, 2008; Drouin *et al.*, 2009; Miller *et al.*, 2009), and Pineto ophiolite (Sanfilippo & Tribuzio, 2012), but shifted towards higher Forsterite values of olivine (Fig. 14b).

Clinopyroxene Mg-number (mol%) shows similar correlations with plagioclase Anorthite (mol%) (Fig. 14c), with relatively constant Mg-number in *Troctolite A* and *Troctolite B* (Mg# = 87.7-91.0 mol%) at varying Anorthite content (An = 55.1-67.0 mol%), similar to mineral compositions analyzed at the easternmost South-West Indian Ridge (61-67°E) (Paquet *et al.*, 2016). The *Gabbroic intrusions* show a positive correlation between Mg-number in clinopyroxene and Anorthite content in plagioclase (from $An_{51.6}$-$Mg\#_{83.7}$ to $An_{62.7}$-$Mg\#_{90.1}$). The slope defined by the Anorthite – Mg-value (cpx) covariation in *Gabbroic intrusions* is consistent with the trends documented in the oceanic gabbroic suites at the Mid-Atlantic Ridge (Ross & Elthon, 1997; Lissenberg & Dick, 2008; Suhr *et al.*, 2008; Drouin *et al.*, 2009; Miller *et al.*, 2009; Ferrando *et al.*, 2018), South-West Indian Ridge (Dick *et al.*, 2002), and in the Pineto gabbroic crust (Sanfilippo & Tribuzio, 2012), but shifted towards higher Mg-values of clinopyroxene (Fig. 14c). Also reported is the compositional field of Alpine-Apennine troctolites, olivine gabbros and gabbros (Hébert *et al.*, 1989; Tribuzio *et al.*, 1999; Montanini *et al.*, 2008; Sanfilippo & Tribuzio, 2012), characterized by lower Anorthite contents in plagioclase at a given Mg-value in clinopyroxene, compared to oceanic gabbroic series (Fig. 14c; SWIR Hole 735B: Dick et al., 2002; MAR Hole U1309D: Ross & Elthon, 1997; Lissenberg & Dick, 2008; Suhr *et al.*, 2008; Drouin *et al.*, 2009; Miller *et al.*, 2009; Ferrando *et al.*, 2018).

8. DISCUSSION

8.1. Replacive origin of the Troctolite A

As documented in previous studies and herein, the Erro-Tobbio troctolitic body crosscuts the host impregnated *Plagioclase lherzolites* and associated pyroxenite banding (Fig. 4; Borghini & Rampone, 2007; Borghini *et al.*, 2007; Rampone *et al.*, 2016), includes *Dunite pods* and develops wehrlite and troctolite apophyses into the mantle *Plagioclase Lherzolites* (Fig. 2a). The *Troctolite A* shows a strong textural complexity with the occurrence of two distinct types of olivines within single samples (Fig. 6a,b,c,d), i.e. millimetre-size undeformed granular olivine grains (Fig. 5a,b) and coarse (up to centimetre-size), deformed and corroded crystals (Fig. 5c,d). As inferred in oceanic settings during formation of olivine-rich troctolites (Suhr *et al.*, 2008; Drouin *et al.*, 2010), Rampone *et al.* (2016) interpreted the textural complexity of the Erro-Tobbio troctolites as the result of melt-rock interactions leading to the dissolution of the olivine matrix and crystallization of interstitial plagioclase. Although they were not able to distinguish two olivine generations in a specific troctolite sample, they inferred that the millimetre-size undeformed granular olivine grains could represent a second generation of "*olivine 2*", whether of magmatic origin or representing disrupted coarse olivine grains. Detailed EBSD analysis (size, shape, misorientation; Fig. 6) allows us to interpret the coarse deformed and corroded olivine as the pre-existing, possibly mantle relict "*olivine 1*". The occurrence of coarse corroded grains almost disrupted into several granular olivines (Fig. 5c) suggests that most of the small undeformed olivine grains are formed after extensive corrosion and disruption of the coarsed pre-existing olivines. This process of textural evolution of the olivine matrix during progressive melt-rock interaction and replacive formation of olivine-rich troctolites has been previously inferred in oceanic settings (Suhr *et al.*, 2008; Drouin *et al.*, 2010; Ferrando *et al.*, 2018) and recently demonstrated in ophiolitic settings at the Mt.Maggiore peridotitic body (Basch *et al.*, 2018).

At the scale of the sample, the *Troctolite A* is also characterized by variations in the texture of the olivine matrix (taken as a whole, *olivines 1* + *olivines 2*), between samples characterized by plagioclase-free dunitic aggregates surrounded by interstitial phases (Fig. 6a,b,c), and disaggregated samples where single olivines are completely embedded in poikilitic plagioclase (Fig. 6d). This textural variability is well correlated with a change in olivine CPO. The olivine matrix of *Troctolite A* characterized by plagioclase-free dunitic aggregates shows an axial-[100] fabric (Fig. 8), similar to the *Spinel lherzolites* and *Dunite pods*. This axial-[100] CPO is typically reported in natural peridotites deformed under asthenospheric conditions (e.g., Tommasi *et al.*, 2000; Le Roux *et al.*, 2008; Soustelle *et al.*, 2009), and indicates that plastic deformation was related to dislocation creep with joint activation of (010)[100] and (001)[100] slip systems, the most easily activated at high temperature conditions (1100-1200°C) (Ben Ismail & Mainprice, 1998; Tommasi *et al.*, 2000; Karato *et al.*, 2008; Drouin *et al.*, 2010; Higgie & Tommasi, 2012). The samples characterized by a disaggregated olivine matrix, embedded in poikilitic plagioclase, show scattered orientations of [100] and [010] olivine axes, and a stronger concentration of the [001] axis (Fig. 8). Such olivine CPOs have been previously reported in zones of melt accumulation in the Oman Moho Transition Zone (Ceuleneer & Rabinowicz, 1992; Boudier & Nicolas, 1995; Jousselin *et al.*, 1998; Dijkstra *et al.*, 2002; Higgie & Tommasi, 2012) and during the replacive formation of olivine-rich troctolites at the Atlantis Massif (Drouin *et al.*, 2010). It has been interpreted as a loss of cohesion of the solid matrix during impregnation at high melt/rock ratios (20-40% melt fraction; Rosenberg & Handy, 2005). Melt-rock interaction microstructures, indicating the corrosion of the pre-existing olivine matrix, together with the preservation of dunitic pods within the host *Troctolite A* (Figs. 2d, 4) and the correlation between the observed texture of the olivine matrix and its CPO (Fig. 8), suggest a replacive formation of *Troctolites A*. We infer that they formed from a mantle *Dunite* protolith (itself preserving the mantle precursor axial-[100] CPO), after reactive percolation of a MORB-type melt at variable melt/rock ratios (Fig. 15). The disaggregation of the olivine matrix associated to the loss of the olivine axial-[100] CPO are indicative of high instantaneous melt-rock ratios (>20-40%; Rosenberg & Handy, 2005), whereas the samples preserving the mantle olivine CPO indicate a reactive percolation at lower melt/rock ratios (Fig. 15). Texture and CPO analyses, together with the occurrence of preserved dunitic pods within the *Troctolite A* thus indicate that *Troctolites A* are likely the replacive product of reactive percolation and impregnation of a pristine dunitic matrix by melts crystallizing plagioclase and minor clinopyroxene.

Peculiar geochemical compositional trends of the rock-forming minerals, not consistent with a simple fractional crystallization process, support the replacive origin of the *Troctolites A*. Despite strong variations in olivine modal compositions (from 55 vol% in troctolites to 97 vol% in dunitic pods), olivines and clinopyroxenes in the *Dunite* and the *Troctolite A* show a narrow range of composition (Fo = 88.2-89.1 mol%; Figs. 10a, 14b; Mg# = 89-91 mol%; Fig. 14c). These constant compositions of the mafic minerals (Forsterite in olivine and Mg-value in clinopyroxene) are coupled with significant within-sample variations in plagioclase Anorthite contents (An = 52.9-66.8 mol%; Fig. 14a,b), and therefore do not follow the compositional trends of fractional crystallization defined by the oceanic gabbroic sequences (South-West Indian Ridge, Dick *et al.*, 2002; Mid-Atlantic Ridge, Ross & Elthon, 1997; Lissenberg & Dick, 2008; Suhr *et al.*, 2008; Drouin *et al.*, 2009; Miller *et al.*, 2009). These peculiar compositional trends (Fig. 14a,b) are indicative of the buffering of the melt Mg-value by olivine-dissolving reactive porous flow percolation (e.g. Collier & Kelemen, 2010; Sanfilippo et al., 2016b; Borghini *et al.*, 2018). Mineral compositions in *Troctolite A* are similar to those documented in the amagmatic easternmost South-West Indian Ridge troctolites and olivine gabbros (61-67°E; Paquet *et al.*, 2016). These peculiar mineral chemistry co-variations were attributed to melt-rock interaction processes involving olivine and orthopyroxene dissolution by a percolating Na-rich basic melt, and subsequent crystallization of plagioclase and clinopyroxene.

8.2. Thermodynamic model of olivine-consuming reactive crystallization

To better constrain and quantify the role of reactive crystallization in the formation of the peculiar An-Fo and An-Mg# compositional trends in the Erro-Tobbio troctolitic body (Fig. 14a,b), we performed an assimilation – fractional crystallization (AFC) geochemical modeling assuming variable dissolved mass of olivine and concomitant melt crystallization, using the *pMELTS* thermodynamic program (Ghiorso *et al.*, 2002). This model aims at reproducing the diffuse reactive percolation of a high-temperature melt (1270°C) into the shallow lithospheric mantle. Based on mineral-mineral partitioning, Rampone *et al.* (2016) documented high temperature of equilibration (> 1100-1200°C) in both troctolites and host peridotites. The interaction process thus occurred at relatively high mantle temperatures.

The Erro-Tobbio ultramafic body does not include any basaltic intrusion, precluding direct information on the *Troctolite A* parental melt composition. However, few unaltered primitive basaltic intrusions (LOI < 2%; Mg# > 70 mol%) have been documented in the Alpine-Apennine ophiolites. The initial melt composition used is a primitive MORB-type basalt (Mg# = 70.75 mol%) associated to the Pineto gabbroic suite (Saccani *et al.*, 2008; Alpine ophiolite), which composition is given in Table 7. This primitive melt is characterized by a relatively low Ca/Na ratio (Ca# = 61.54 mol%), most likely as the result of low degrees of mantle melting (Klein & Langmuir, 1987; Montanini *et al.*, 2008; Saccani *et al.*, 2008; Renna *et al.*, 2018), similarly to what was described at the easternmost South-West Indian Ridge (Ca# = 55-60 mol%; Paquet *et al.*, 2016). Such a Na-rich parental melt composition is consistent with the Alpine-Apennine compositional field of gabbroic rocks (Fig. 14c; Hébert *et al.*, 1989; Tribuzio *et al.*, 1999; Montanini *et al.*, 2008; Sanfilippo & Tribuzio, 2012), showing more Na-rich plagioclase compositions (at given Mg-value in clinopyroxene) than the oceanic gabbroic series at the South-West Indian Ridge and Mid-Atlantic Ridge (Fig. 14c).

We modelled isobaric (P = 4 kbar) reactive fractional crystallization of the primitive MORB melt, cooling at steps of 5°C while dissolving a fixed mass of olivine (0g, 1g, 2g, 3g per 100g of melt) per 1°C of cooling (Fig. 16). Similar models of reactive crystallization using the *pMELTS* thermodynamic program (Ghiorso *et al.*, 2002) have been previously performed by Collier & Kelemen (2010) and Sanfilippo *et al.* (2016), involving the assimilation of mantle lherzolites at 6 kbar. In the Erro-Tobbio, the *Troctolite A* includes decimetre-size dunitic pods (Fig. 2d) preserved from melt impregnation and no mantle pyroxene relict is found in any dunite or troctolite sample. This suggests that the protolith of the Erro-Tobbio troctolite was a *Dunite*. Microstructures in *Troctolite A* indicate the late crystallization of poikilitic clinopyroxene in minor proportions (Table 1; Fig. 5b), therefore suggesting relatively low crystallization pressures (<7kbar), leading to the late saturation of clinopyroxene on a MORB-type melt liquid line of descent (Husen *et al.*, 2016). Based on field, microstructural observations, and previous geobarometric estimates within the *Troctolite A* (3-5 kbar; Borghini *et al.*, 2007), we decided to model the dissolution of 100% olivine Fo_{89} (olivine composition in the *Dunite* pods) at variable assimilation rates (see below) during a reactive fractional crystallization process occurring at 4 kbar. Recent experimental work (Borghini *et al.*, 2018; Francomme, 2018) demonstrated the possible replacive formation of an olivine-rich troctolite from a dunite protolith and the efficient buffer of the melt composition towards high Mg-values by olivine assimilation. They also demonstrated that the reactivity of a melt saturated in olivine (AH6; Husen *et al.*, 2016) with a dunitic matrix Fo_{90} is driven by the chemical disequilibrium between the olivine forming the dunitic matrix (more forsteritic) and the olivine in equilibrium with the melt (see also Liang, 2003). The partial dissolution of the dunitic matrix is thus associated with the precipitation of an olivine of different composition that is in equilibrium with the modified melt.

Figure 16 shows the computed crystal line of descent of olivine, plagioclase and clinopyroxene and Table S6 reports the evolution of the melt and mineral compositions during fractional and reactive crystallization. The computed crystallization order is [olivine-plagioclase-clinopyroxene], as expected from the crystallization of a MORB melt at low pressures (<7 kbar; Bender *et al.*, 1978; Husen *et al.*, 2016). The starting melt composition is in equilibrium with an olivine Fo = 87 mol%, but at increasing dissolution rates (from 0g/°C to 3g/°C of cooling), the equilibrium Forsterite content in olivine and the Mg-value in clinopyroxene are progressively buffered by the composition of the dissolved olivine (Fo = 89 mol%). It is worth noting that this extensive olivine dissolution implies the crystallization of new olivine crystals and/or recrystallization of the olivine matrix all along the reactive percolation process (Table S6; Liang, 2003). Table S6 shows that even at high dissolution rates (3g/°C of cooling), the early stages of reactive crystallization (1270-1260°C) characterized by crystallization of olivine only, do not involve a significant variation in melt mass (olivine dissolved/olivine crystallized = 0.88-1.12). This supports the dissolution-reprecipitation of the pre-existing dunitic matrix. Moreover, given that in the *Troctolite A*, most small undeformed olivine crystals embedded in poikilitic plagioclase and clinopyroxene are the result of extensive corrosion and disruption of large olivine grains (and therefore do not represent newly formed magmatic olivines; see previous **Discussion 8.1**), it is likely that olivine precipitation mostly consisted in the recrystallization of the pre-existing olivine rims (Liang, 2003; Morgan & Liang, 2005). However, no compositional variation was found between the olivine cores (possibly relict) and rims (possibly recrystallized) (Fig. 12i-l). This is presumably due to similar composition of the pre-existing (Fo = 89 mol%; Table 2) and recrystallized olivine (Fo ≈ 88 mol%; Table S6), and to the fast Mg-Fe diffusion rates of olivine at magmatic temperatures (t_{equ} < 200 years for 3 mm radius; Dohmen & Chakraborty, 2007; Ferrando *et al.*, 2018).

During the reactive fractional crystallization process, the Anorthite contents in plagioclase evolve freely towards lower values along the crystal line of descent (Fig. 16), leading to the reactive crystallization trends of variation previously described by Collier & Kelemen (2010) and Sanfilippo et al. (2016) (decreasing Anorthite contents in plagioclase at constant Forsterite contents in olivine and Mg-value in clinopyroxene). Crystal lines of descent at high rates of olivine dissolution during reactive crystallization (from 2g/°C to 3g/°C of cooling) fit well the analyzed peculiar trends of mineral covariation in the Erro-Tobbio troctolites and confirms the strong implication of olivine-dissolving reactive porous flow processes in the formation of the *host Troctolite A* from a pre-existing dunite (Figs. 15, 16).

Clinopyroxene cores from the *Troctolite A* show high Cr_2O_3 contents (Fig. 11a,c), similar to those described in oceanic gabbroic rocks analyzed at the Mid-Atlantic Ridge (Lissenberg & Dick, 2008; Lissenberg & MacLeod, 2016; Ferrando *et al.*, 2018), easternmost South-West Indian Ridge (Paquet *et al.*, 2016) and Godzilla Megamullion (Sanfilippo *et al.*, 2016b), and in olivine-rich troctolites from the Internal Liguride ophiolite (Renna & Tribuzio, 2011; Renna *et al.*, 2016). Although *pMELTS* (Ghiorso *et al.*, 2002) does not allow the Cr_2O_3 compositional modeling of clinopyroxene, the process of partial dissolution and recrystallization of a dunite (olivine + spinel) described above could well explain the Cr_2O_3 enrichments observed in the clinopyroxene cores (Fig. 11a,c). Within *Troctolite A*, interstitial minerals often develop embayments on corroded relict of spinel grains. This indicates partial dissolution of Cr-rich spinel (Cr# = 55-65 in the dunite; Table 6) together with the olivine during the reactive melt percolation process, as was previously described in oceanic settings and in the Internal Liguride ophiolites during replacive formation of olivine-rich gabbroic rocks (Lissenberg & Dick, 2008; Renna & Tribuzio, 2011; Lissenberg & MacLeod, 2016; Paquet *et al.*, 2016; Renna *et al.*, 2016; Sanfilippo *et al.*, 2016b; Ferrando *et al.*, 2018). The corrosion of spinel leads to Cr_2O_3 enrichments in the reacting melt, therefore explaining the Cr-rich compositions of clinopyroxenes crystallized from the percolating modified melt (Fig. 11a). The corrosion of spinel during impregnation of the dunite and the Cr-rich character of the melt is also suggested within *Troctolite A* by the crystallization of numerous fine-grained euhedral spinels associated with the poikilitic plagioclase (Fig. 6d).

8.3. Magmatic origin of Troctolite B

The *Troctolite B* pseudotabular bodies crosscut the *Troctolite A* structures, with irregular to straight contacts with the host troctolite (Figs 2c, 3a,b, 4). *Troctolites B* have lower modal contents of olivine (from 45 to 60 vol% modal olivine), with respect to the *host Troctolite A* (from 55% to 97% modal olivine). The olivine matrix within *Troctolite B* shows extreme textural variations (Figs. 3b,c,d,e, 6e), from millimetre-size euhedral (Fig. 7a) to centimetre-size hopper (Fig. 7b) to centimetre- to decimetre-size skeletal and dendritic crystals (Fig. 7c,d) (Rampone *et al.*, 2016). Hopper and dendritic morphologies of olivine have been previously described in the Rum Layered Intrusion (Donaldson, 1974, 1977, 1982; O'Driscoll *et al.*, 2007), in olivine-rich troctolites from the

Ligurian ophiolites (Renna *et al.*, 2016) and in crystallization experiments (Donaldson, 1976, 1977; Faure *et al.*, 2003, 2007) as resulting from a rapid disequilibrium crystallization of an undercooled melt (driven by a difference between the liquidus temperature of the melt and the melt temperature).

Olivine CPO in the granular portion of the *Troctolite B* shows random orientations of the [100] axis, strong concentrations of the [010] axis normal to the foliation, and [001] axis being the strongest axis concentration within the foliation plane (Fig. 9). In *Gabbroic intrusions*, similar olivine CPOs are observed, correlated with strong orientations of plagioclase [010] axis normal to the foliation plane (parallel to the [010] axis of olivine) (Fig. 9). Benn & Allard (1989) and Jousselin *et al.* (2012) previously described such CPOs of olivine in the Oman lower crustal layered gabbros and interpreted these orientations as the shape-related physical orientation of the crystals during magmatic flow.

Based on the crosscutting relationships between *Troctolite B* and the *host Troctolite A* (Figs. 2b, 3a,c), the textural variability of olivine (Figs. 3b,c,d,e, 6e), and the CPO indicative of magmatic flow within the granular part of the *Troctolite B* (Fig. 9), we infer that the *Troctolite B* originated as a magmatic segregation within the hot pre-existing *Troctolite A* during focused percolation of the melt modified after the diffuse reactive percolation forming the *Troctolite A* (see the modeling below). The irregular contacts between the *Troctolite B* intrusions and the host *Troctolite A* indicate a brittle-ductile rheological behaviour, thus suggesting a minor temperature difference (<50°C) between the system and the intruding melt. The rheological evolution from diffuse percolation (forming *Troctolite A*) to focused percolation (related to a slight decrease in the temperature of the system) allowed higher quantities of melt to segregate and to form a magmatic flow (Fig. 9), leading to the crystallization of the *Troctolite B*.

The mineral major elements compositions of olivine, plagioclase and clinopyroxene in *Troctolite B* are less variable than in *Troctolite A*. The Forsterite contents in olivine (Fo = 87.3-89.2; Figs. 10a, 14b,c), the Mg-values (Mg# = 88.2-91; Figs. 11, 14a,c) and Cr_2O_3 contents in clinopyroxene (up to Cr_2O_3 = 1.55 wt%; Fig. 11a,c), and the Anorthite contents in plagioclase (An = 55.1-66.1; Fig. 14) are in the same range of composition as previously described in *Troctolite A*. The geochemical model (using *pMELTs*; Ghiorso *et al.*, 2002) of reactive fractional crystallization developed for the *host Troctolite A* (Fig. 16) also fits the major element compositions of the *Troctolite B* mineral couples, showing constant Forsterite contents in olivine and Mg-values in clinopyroxene at decreasing Anorthite contents in plagioclase (Figs. 14b,c, 16). This indicates that the magmatic *Troctolite B* crystallized from the melt modified after the diffuse reactive percolation originating the *Troctolite A*. Table 7 reports the initial melt composition and liquidus temperature of the Pineto primitive MORB melt used in the thermodynamic model of fractional and reactive crystallization (see **Discussion 8.2**), and the modified melt composition and liquidus temperature computed using *pMELTs* (Ghiorso *et al.*, 2002), after dissolution of 5, 10, and 15 grams of olivine (corresponding to a 5°C step of cooling for the modelled 1g/°C, 2g/°C and 3g/°C; Fig. 16). It should be noted that the modified compositions reported in Table 7 consider only the dissolution of the olivine matrix during a 5°C cooling step, and not the subsequent precipitation of olivine from the melt. This approach allows to compute the maximum increase in liquidus temperature driven by olivine assimilation (Table 7) in the modified melts, and therefore to assess the maximum degree of undercooling developed prior to olivine reprecipitation. The dissolution of olivine leads to a local increase of the Mg-value of the melt, resulting in an increase of the liquidus temperature of the melt up to 83°C (relative to the liquidus temperature of the initial melt), for the assimilation of 15 grams of olivine during one 5°C step of cooling (3g/°C of cooling; Ghiorso *et al.*, 2002; Table 7). Hence, the described process of partial dissolution of the olivine matrix is able to rapidly develop a significant degree of undercooling of the melt, by increasing its liquidus temperature at almost constant melt temperature. We infer that the textural variability of olivine observed within the magmatic *Troctolite B* is the result of local changes in the degree of undercooling of the segregated melt, as was previously described in the Rum layered intrusion (Donaldson, 1974, 1976, 1977, 1982; O'Driscoll *et al.*, 2007). Crystallization experiments of mafic/ultramafic melts performed over a range of degrees of undercooling and cooling rates (Donaldson, 1976, 1977, Donaldson *et al.*, 1975; Faure *et al.*, 2003, 2007) highlighted the possible development of hopper and dendritic olivine morphologies at degrees of undercooling as low as 10-20°C. Olivine dissolution involved in the reactive formation of *Troctolite A* is therefore a very good candidate to explain the skeletal and dendritic morphologies of magmatic olivine crystallized in *Troctolite B*.

The lack of significant geochemical variation between the different olivine morphologies (granular, hopper and skeletal) precludes the identification of a clear scenario for their formation sequence. However, slightly more evolved major elements composition of olivine (Fo = 87.5-88, Fig. 10), plagioclase (An = 60-62, Fig. 13) and clinopyroxene (Mg# = 88.7-89.5) in the granular part of *Troctolite B* (MF46A, Table 1) possibly implies a late crystallization, after the rapid growth of skeletal dendritic olivines. Moreover, O'Driscoll *et al.* (2007) previously proposed for the Rum layered intrusion that the absence of initial suspended olivine in the primitive magmatic flow may favour the development of a melt undercooling. These arguments point to a model of formation of *Troctolite B* where dendritic olivines rapidly formed in the undercooled melt, prior to its evolution and crystallization of the granular olivines (Fig. 17).

8.4. Intrusion of the modified melt – Formation of the Gabbroic intrusions

Gabbroic intrusions crosscut both the troctolitic body and the associated impregnated *Plagioclase lherzolites* and show straight contacts with their host rock (Borghini & Rampone, 2007; Borghini *et al.*, 2007; Rampone *et al.*, 2016). Olivines and plagioclases from *Gabbroic intrusions* show CPO consistent with the shape-related orientation of the crystals in a magmatic flow (Benn & Allard, 1989; Jousselin *et al.*, 2012). Major elements compositions of the rock-forming minerals (Forsterite content in olivine, Anorthite content in plagioclase and Mg-value in clinopyroxene) show a positive correlation and an evolution following a fractional crystallization trend, parallel to the compositional trends reported for oceanic gabbroic series at the Mid-Atlantic Ridge (Fig. 14b,c) (Ross & Elthon, 1997; Lissenberg & Dick, 2008; Suhr *et al.*, 2008; Drouin *et al.*, 2009; Miller *et al.*, 2009; Ferrando *et al.*, 2018) and the South-West Indian Ridge (Dick *et al.*, 2002). However, although showing similar mineral geochemical trends of evolution to the oceanic gabbroic series, their compositions are shifted towards higher Forsterite contents in olivine and Mg-value in clinopyroxene at a given Anorthite content in plagioclase (Fig. 14b,c). The most primitive *Gabbroic intrusions* show mineral major element compositions similar to those analyzed in *Troctolite B*, thus indicating a common parental melt. Accordingly, we infer that *Gabbroic intrusions* formed by fractional crystallization of the melt modified after the reactive fractional crystallization that formed *Troctolites A* and *B* (Fig. 16), at lower temperatures allowing for brittle behaviour and emplacement of the melt in fractures (Borghini *et al.*, 2007; Rampone & Borghini, 2008).

In order to test this hypothesis, we performed a geochemical modelling of fractional crystallization (using *pMELTS;* Ghiorso *et al.*, 2002) using as a starting melt the output modified melt composition after previous reactive fractional crystallization (Fig. 18, Table 7). As shown in Figure 18, the fractional crystallization of the modified melt reproduces the chemical covariation arrays observed in *Gabbroic intrusions*, almost parallel to the trends defined by oceanic gabbroic suites but shifted towards Mg-rich mineral compositions of olivine (Forsterite content) and clinopyroxene (Mg-value). This confirms that the *Gabbroic intrusions* parental melt corresponds to the melt modified after formation of *Troctolites A* and *B*, and that no further melt-rock interaction was involved in the fractional crystallization process.

8.5. Constraints on the geodynamic context and melt-rock interaction processes

Geochronological data on the Erro-Tobbio gabbroic intrusions (Sm-Nd, 178 ± 5 Ma; Rampone *et al.*, 2014), together with gabbroic rocks in the External Liguride units (170-179 Ma Northern Apennines; Tribuzio *et al.*, 2004), yield the oldest ages available for the gabbroic crust of the

Ligurian Tethys ocean. These ages are older than the continental break-up and onset of oceanization of the Ligurian Tethys (164-166 Ma; Manatschal & Müntener, 2009). Also, they indicate a ~10 Ma time gap between the early emplacement of the Erro-Tobbio and External Liguride gabbros, and the main magmatic activity of the Ligurian Tethys (155-165 Ma; Rampone *et al.*, 2014 and references therein). Accordingly, the Erro-Tobbio gabbroic intrusions have been interpreted as an early magmatism in thinned lithospheric mantle exhumed at ocean-continent transition settings during the onset of the Jurassic lithospheric extension (Fig. 19a; Manatschal & Müntener, 2009; Rampone *et al.*, 2014). The scarcity of gabbroic and basaltic bodies found in the Alpine-Apennine ophiolites (e.g. Marroni *et al.*, 1998; Tribuzio *et al.*, 2000, 2004; Montanini *et al.*, 2008; Saccani *et al.*, 2008), and the Na-rich composition of the basaltic parental melts (Fig. 14c; Saccani *et al.*, 2008; see **Discussion 8.2**) are consistent with low degree of melting of the upwelling mantle in a slow- to ultra-slow spreading environment (Klein & Langmuir, 1987; Montanini et al., 2008; Saccani et al., 2008; Renna et al., 2018; Fig. 19a).

Our structural data, showing the partial preservation of the protolith axial-[100] olivine CPO during replacive formation of the *Troctolite A* (Fig. 8), point to a percolation process occurring at variable instantaneous melt/rock ratios, in an overall low melt supply regime (Fig. 15; see **Discussion 8.1**). Also, our thermodynamic models show that extensive dissolution-precipitation reactions are needed during the multi-stage formation of *Troctolite A* and *Troctolite B* to explain their peculiar compositional trends (Figs. 16, 19b; see **Discussion 8.2, 8.3**). As demonstrated by several mass balance and Assimilation Fractional Crystallization models (Lissenberg & Dick, 2008; Sanfilippo *et al.*, 2015b; Paquet *et al.*, 2016; Rampone *et al.*, 2016), modifications of the melt composition during melt-rock interactions are only possible at low melt supply conditions. Chemical core-rim profiles in interstitial phases from *Troctolite A* (plagioclase and clinopyroxene, Fig. 12a-h) show decreasing Cr_2O_3 and Al_2O_3, and increasing TiO_2 concentrations in clinopyroxene towards the rim (<200µm from the contact with olivine), and decreasing Anorthite content, CaO and Al_2O_3 concentrations towards the plagioclase rim. These core-rim chemical zonations in interstitial clinopyroxene and plagioclase suggest an *in-situ* evolution of the melt composition during reactive crystallization at decreasing melt mass (Borghini & Rampone, 2007; Borghini *et al.*, 2007; Rampone & Borghini, 2008). This indicates that the process forming the replacive *Troctolite A* is not characterized by constant replenishment and efficient extraction of the melt (Fig. 19b), but rather by sparse melt injections which chemical composition were dominated by the dissolution-precipitation processes.

Mineral reactive compositional trends (constant Mg# of olivine and clinopyroxene at variable An content in plagioclase), similar to those observed in the Erro Tobbio troctolitic body, have been documented in olivine-rich troctolites from slow-spreading oceanic environments at the easternmost South-West Indian Ridge (Fig. 16; Paquet *et al.*, 2016) and at the Godzilla Megamullion (Fig. 16; Sanfilippo *et al.*, 2016b). Both these settings are characterized by scarse basaltic and gabbroic intrusions in kilometres of exhumed mantle peridotites. In these troctolites, peculiar compositional trends in minerals were interpreted as the result of extensive melt-rock interaction processes involving low magma supplies and melt/rock ratios (Paquet *et al.*, 2016; Sanfilippo *et al.*, 2016b).

Replacive olivine-rich troctolites were also described at the Atlantis Massif (IODP Hole U1309D; Blackman *et al.*, 2006; Suhr *et al.*, 2008; Drouin *et al.*, 2009, 2010; Ferrando *et al.*, 2018), associated to a 1415-metre-long crustal section (>90% gabbroic rocks; Blackman *et al.*, 2006). Interestingly, the mineral compositions of these olivine-rich troctolites and associated gabbroic crust follow a trend of fractional crystallization at ~2kbar (Miller *et al.*, 2009). This indicates that the global composition of the percolating MORB melt was not modified during the melt-rock interaction processes and formation of replacive olivine-rich troctolites (Ferrando *et al.*, 2018). Consistently, structural data of the olivine CPO within olivine-rich troctolites from Atlantis Massif suggest high melt supply and melt/rock ratios involved in the melt percolation and dissolution-precipitation reactions (Drouin *et al.*, 2010; Ferrando *et al.*, 2018). This further confirms that low melt/rock ratios are necessary to drive a significant modification of the melt composition during melt-rock interaction processes.

The context of formation of the Erro-Tobbio troctolitic body and associated gabbroic intrusions is therefore representative of a slow- to ultraslow-spreading system characterized by very low melt supply, and therefore allowing the percolating melt composition to be controlled and buffered by the melt-rock interaction processes.

9. SUMMARY AND CONCLUSIONS

In the studied field, the Erro-Tobbio peridotites, troctolites and gabbroic intrusions record a multi-stage structural and geochemical evolution involving extensive dissolution-precipitation reactions. It can be summarized as follows: i) The formation of the replacive *Troctolite A* is related to diffuse reactive melt percolation in a pre-existing dunitic matrix (Fig. 19b). Mineral compositions in *Troctolite A* and thermodynamic models indicate a melt-rock interaction-dominated process (Fig. 16), which involves olivine dissolution and crystallization of plagioclase and minor clinopyroxene; ii) Subsequently, the focussing of melts modified after reactive percolation leads to the formation of pseudo-tabular *Troctolite B* magmatic bodies (Fig. 19b). High degrees of undercooling in the modified melt result in hopper to dendritic olivine morphologies during crystallization of *Troctolite B* (Fig. 17); iii) The late gabbroic dykes, crosscutting the association between the impregnated plagioclase peridotites and *Troctolite A* and *B*, represent the product of fractional crystallization of the same modified melts (Fig. 19b).

The evolution from diffuse reactive percolation to focused reactive percolation, followed by intrusion and fractional crystallization of the *Gabbroic intrusions*, is driven by the decreasing temperature of the exhuming system (Fig. 19a), ruling the rheology of the host rock and the ability of the melt to segregate into magmatic intrusions. The geochemical similarities observed between *Troctolite B* and the most primitive *Gabbroic intrusions* indicate a common modified parental melt, which allows to link the focused percolation and intrusion events. Thus, the multi-stage formation of the troctolitic body and associated gabbroic intrusions (Fig. 19b) are related to a single thermal evolution of the ultramafic body, during the onset of opening of the Ligurian Tethys (Fig. 19a).

This study provides field-controlled constraints on the structural and geochemical modifications induced by melt-rock interaction processes, as a function of the involved melt/rock ratio. At low melt supply and melt/rock ratios, the structure of the protolith is preserved during reactive crystallization, while the melt composition can be easily controlled by the ongoing dissolution-precipitation reactions. This leads to the observed buffer of the melt composition towards high Mg-values in the troctolitic body. In contrast, melt percolation involving high melt supply and melt/rock ratios leads to the loss of cohesion of the solid matrix and pre-existing structure. In such circumstances, the global melt composition cannot be modified during melt-rock interactions and the crystallized minerals follow a fractional crystallization trend, as documented at the Atlantis Massif.

Acknowledgements:

We would like to thank Prof. Joerg Hermann, Dr. Alessio Sanfilippo and an anonymous reviewer for their constructive comments and the increase of the quality of the manuscript. We also thank Paolo Campanella and Alessandra Gavoglio, Christophe Nevado and Doriane Delmas for realisation of the thin section and high-quality polishing, as well as Fabrice Barou for assistance with the EBSD analyses, Andrea Risplendente for assistance with the EPMA analyses, Marco Scarsi and Nicola Campomenosi for assistance with field work, and Giulio Borghini for stimulating discussions. This project has been supported by the People Programme (Marie Curie Actions) of the European Union's Seventh Framework Programme FP7/2007-2013/ under REA-Grant Agreement No. 608001, "ABYSS", and by the Italian Ministry of Education, University and Research (MIUR)

[PRIN-2015C5LN35] “Melt-rock reaction and melt migration in the MORB mantle through combined natural and experimental studies”.

References

Basch, V. (2018) Melt-rock interactions in the oceanic lithosphere: microstructural and petro-geochemical constraints from ophiolites. *PhD thesis, IRIS (Institutional Research Information System)*, doi: 10.15167/basch-valentin_phd2018-05-10.

Basch, V., Rampone, E., Crispini, L., Ferrando, C., Ildefonse, B. & Godard, M. (2018). From mantle peridotites to hybrid troctolites: textural and chemical evolution during melt-rock interaction history (Mt.Maggiore, Corsica, France). *Lithos,* doi: 10.1016/j.lithos.2018.02.025.

Bender, J. F., Hodges, F. N. & Bence, A. E. (1978). Petrogenesis of basalts from the project FAMOUS area: experimental study from 0 to 15 kbars. *Earth and Planetary Science Letters,* **41**, 277-302, doi: 10.1016/0012-821X(78)90184-X.

Ben Ismail, W. & Mainprice, D. (1998). An olivine fabric database: an overview of upper mantle fabrics and seismic anisotropy. *Tectonophysics,* **296**, 145-157, doi: 10.1016/S0040-1951(98)00141-3.

Benn, K. & Allard, B. (1989). Preferred mineral orientations related to magmatic flow in ophiolite layered gabbros. *Journal of Petrology,* **30**, 925-946, doi: 10.1093/petrology/30.4.925.

Bezzi, A. & Piccardo, G. B. (1971). Structural features of the Ligurian ophiolites: Petrologic evidence for the ‘oceanic’ floor of the Northern Apennines geosyncline: A contribution to the problem of the alpine-type gabbro-peridotite associations. *Memorie della Società Geologica Italiana*, **10**, 53–63.

Blackman, D. K., Ildefonse, B., John, B. E., Ohara, Y., Miller, D. J., MacLeod, C. J. & Expedition 304/305 Scientists (2006). Expedition 304/305. *Proceedings of the Integrated Ocean Drilling Program*, **304/305**, doi: 10.2204/iodp.proc.304305.101.2006.

Borghini, G. & Rampone, E. (2007). Postcumulus processes in oceanic-type olivine-rich cumulates: the role of trapped melt crystallization versus melt-rock interaction. *Contributions to Mineralogy and Petrology* **154**, 619-633, doi: 10.1007/s00410-007-0217-5.

Borghini, G., Rampone, E., Crispini, L., De Ferrari, R. & Godard, M. (2007). Origin and emplacement of ultramafic–mafic intrusions in the Erro-Tobbio mantle peridotite (Ligurian Alps, Italy), *Lithos*. **94**, 210-229. doi: 10.1016/j.lithos.2006.06.014.

Borghini, G., Francomme, J. E. & Fumagalli, P. (2018). Melt-dunite interactions at 0.5 and 0.7GPa: experimental constraints on the origin of olivine-rich troctolites. *Lithos*, doi: 10.1016/j.lithos.2018.09.022.

Borsi, L., Scharer, U., Gaggero, L. & Crispini, L. (1996). Age, origin and geodynamic significance of plagiogranites in lherzolites and gabbros of the Piedmont-Ligurian ocean basin. *Earth and Planetary Science Letters,* **140**, 227-241, doi: 10.1016/0012-821X(96)00034-9.

Boudier, F. & Nicolas, A. (1995). Nature of the Transition Zone in the Oman Ophiolite. *Journal of Petrology*, **36**, 777-796, doi: 10.1093/petrology/36.3.777.

Bunge, H. J. (1982) Texture analysis in material sciences. *Butterworths, London*

Capponi, G., Crispini, L., Silvestri, R. & Vigo, E. (1999). The role of Early Miocene thrust tectonics in the structural arrangement of the Voltri Group (Ligurian Alps, Italy): evidence of Bandita area. *Ofioliti,* **24**, 13-19.

Ceuleneer, G. & Rabinowicz, M. (1992). Mantle flow and melt migration beneath oceanic ridges: Models derived from observation in ophiolites, in mantle flow and melt generation at mid-ocean ridges, *Geophysical Monograph Series,* **71**, edited by J. P. Morgan, D.B. Blackman, and J.M. Sinton: 123-154, AGU, Washington, D. C.

Collier, M. L. & Kelemen, P. B. (2010). The Case for Reactive Crystallization at Mid-Ocean Ridges, *Journal of Petrology*, **51**, 1913-1940, doi: 10.1093/petrology/egq043.

Chiesa, S., Cortesogno, L., Forcella, F., Galli, M., Messiga, B., Pasquarè, G., Pedemonte, G. M., Piccardo, G. B. & Rossi, P. M. (1975). Assetto strutturale ed interpretazione geodinamica del Gruppo di Voltri. *Bolletino della Società Geologica Italiana*, **94**, 555-581.

Coumans, J. P., Stix, J., Clague, D. A., Minarik, W. G. & Layne G. D. (2016). Melt-rock interaction near the Moho: Evidence from crystal cargo in lavas from near-ridge seamounts. *Geochimica et Cosmochimica Acta*, **191**, 139-164, doi: 10.1016/j.gca.2016.07.017.

De Paolo (1981). Trace element and isotopic effects of combined wallrock assimilation and fractional crystallization. *Earth and Planetary Science Letters*, **53**, 189-202, doi: 10.1016/0012-821X(81)90153-9.

Dick, H. J. B. & Natland, J. H. (1996). Late stage melt evolution and transport in the shallow mantle beneath the East Pacific Rise. In: Gillis, K., Mével, C. and Allan, J. (eds.) *Proceedings of the Ocean Drilling Program, Scientific Results*, **147**, 103-134, Ocean Drilling Program, College Station, TX.

Dick, H. J. B., Ozawa, K., Meyer, P. S., Niu, Y., Robinson, P. T., Constantin, M., Hebert, R., Maeda, J., Natland, J. H., Hirth, J. G. & Mackie, S. M. (2002). Primary silicate mineral chemistry of a 1.5-km section of very slow spreading lower ocean crust: ODP Hole 735B, Southwest Indian Ridge. In: Natland JH, Dick HJB, Miller DJ, Von Herzen RP (eds) Proc. ODP, Sci. Results, vol 176, chap 10. Ocean Drilling Program, College Station, Texas, pp 1–61, doi: 10.2973/odp.proc.sr.176.001.2002.

Dick, H. J. B., Tivey, M. A. & Tucholke, B. E. (2008). Plutonic foundation of a slow-spreading ridge segment: Oceanic core complex at Kane Megamullion, 23°30'N, 45°20'W. *Geochemistry, Geophysics, Geosystems*, **9**, Q05014, doi: 10.1029/2007GC001645.

Dick, H. J. B., Lissenberg, C. J. & Warren, J. M. (2010). Mantle melting, melt transport, and delivery beneath a Slow-Spreading Ridge: The Paleo-MAR from 23°15'N to 23°45'N. *Journal of Petrology*, **51**, 425–467, doi: 10.1093/petrology/egp088.

Dijkstra, A. H., Drury, M. R. & Frijhoff, R. M. (2002). Microstructures and lattice fabrics in the Hilti mantle section (Oman Ophiolite): Evidence for shear localization and melt weakening in the crust–mantle transition zone? *Journal of Geophysical Research,* **107**, 2270, doi: 10.1029/2001JB000458.

Dijkstra, A. H., Barth, M. G., Drury, M. R., Mason, P. R. D. & Vissers, R. L. M. (2003). Diffuse porous melt flow and melt-rock reaction in the mantle lithosphere at a slow-spreading ridge: A structural petrology and LA-ICP-MS study of the Othris Peridotite Massif (Greece). *Geochemistry, Geophysics, Geosystems*, **4**, 8613, doi: 10.1029/2001GC000278.

Dohmen, R. & Chakraborty, S. (2007). Fe-Mg diffusion in oivine II: point defect chemistry, change of diffusion mechanisms and a model for calculation of diffusion coefficients in natural olivine. *Physics and Chemistry of Minerals,* **34**, 409-430, doi: 10.1007/s00269-007-0158-6.

Donaldson, C. H. (1974). Olivine crystal types in harrisitic rocks of the Rhum pluton and in Archean spinifex rocks. *Geological Society of American Bulletin,* **85**, 1721-1726, doi: 10.1130/0016-7606(1974)85<1721:OCTIHR>2.0.CO;2.

Donaldson, C. H. (1976). An experimental investigation of olivine morphology. *Contributions to Mineralogy and Petrology*, **57**, 187-213, doi: 10.1007/BF00405225.

Donaldson, C. H. (1977). Laboratory duplication of comb layering in the Rhum pluton. *Mineralogical Magazine*, **41**, 323-336, doi: 10.1180/minmag.1977.041.319.03.

Donaldson, C. H. (1982). Origin of some of the Rhum harrisite by segregation of intercumulus liquid. *Mineralogical Magazine*, **45**, 201-209, doi: 10.1180/minmag.1982.045.337.23.

Donaldson, C. H., Williams, R.J. & Lofgren, G.E. (1975). A sample holding technique for study of crystal growth in silicate melts. *American Mineralogist*, **60**, 324-326.

Drouin, M., Godard, M., Ildefonse, B., Bruguier, O. & Garrido, C. (2009). Geochemical and petrographic evidence for magmatic impregnation in the oceanic lithosphere at Atlantis Massif, Mid-Atlantic Ridge (IODP Hole U1309D, 30°N). *Chemical Geology*, doi: 10.1016/j.chemgeo.2009.02.013.

Drouin, M., Ildefonse, B. & Godard, M. (2010). A microstructural imprint of melt impregnation in slow spreading lithosphere: olivine-rich troctolites from the Atlantis Massif, Mid-Atlantic Ridge, 30°N, IODP Hole U1309D. *Geochemistry, Geophysics, Geosystems,* **11**, Q06003, doi: 10.1029/2009GC002995.

Dygert, N., Liang, Y. & Kelemen, P. B. (2016). Formation of Plagioclase Lherzolite and associated Dunite-Harzburgite-Lherzolite Sequences by multiple episodes of melt percolation and melt rock reaction: an example from the Trinity ophiolite, California, USA. *Journal of Petrology*, **57**, 815-838, doi: 10.1093/petrology/egw018.

Elthon, D. (1987). Mineral chemistry of gabbroic rocks from the Mid-Cayman Rise spreading center, *Journal of Geophysical Research*, **92**, 658-682, doi: 10.1029/JB092iB01p00658.

Ernst, W. G. & Piccardo, G. B. (1979). Petrogenesis of some Ligurian peridotites: I. Mineral and bulk rock chemistry. *Geochimica Cosmochimica Acta*, **43**, 219–237, doi: 10.1016/0016-7037(79)90241-2.

Faure, F., Trolliard, G., Nicollet, C. & Montel, J. M. (2003). A developmental model of olivine morphology as a function of the cooling rate and the degree of undercooling. *Contributions to Mineralogy and Petrology*, **145**, 251-263, doi: 10.1007/s00410-003-0449-y.

Faure, F., Schiano, P., Trolliard, G., Nicollet, C & Soulestin, B. (2007). Textural evolution of polyhedral olivine experiencing rapid cooling rates. *Contributions to Mineralogy and Petrology,* **153**, 405-416, doi: 10.1007/s00410-006-0154-8.

Ferrando, C., Godard, M., Ildefonse, B. & Rampone, E. (2018). Melt transport and mantle assimilation at Atlantis Massif (IODP Site U1309): Constraints from geochemical modelling. *Lithos*, doi: 10.1016/j.lithos.2018.01.012.

Francomme, J. E. (2018) Melt-rock interaction at the mantle-crust transition zone in the oceanic spreading lithosphere: an experimental study. *PhD thesis, IRIS (Institutional Research Information System).*

Garrido, C. J. & Bodinier, J-L. (1999). Diversity of mafic rocks in the Ronda peridotite: Evidence for pervasive melt-rock reaction during heating of subcontinental lithosphere by upwelling asthenosphere. *Journal of Petrology*, **40**, 729-754, doi: 10.1093/petroj/40.5.729.

Ghiorso, M. S., Hirschmann, M., Reiners, P. W. & Kress, V. C. I. (2002). The pMELTS: A revision of MELTS aimed at improving calculation of phase relations and major element partitioning involved in partial melting of the mantle at pressures up to 3GPa. *Geochemistry, Geophysics, Geosystems*, **3**, doi: 10.1029/2001GC000217.

Gillis, K. et al. (2014). Primitive layered gabbros from fast-spreading lower oceanic crust. *Nature*, **505**, 204-207, doi: 10.1038/nature12778.

Godard, M., Bodinier, J-L. & Vasseur, G. (1995). Effects of mineralogical reactions on trace element redistributions in mantle rocks during percolation processes: A chromatographic approach. *Earth and Planetary Science Letters*, **133**, 449-461, doi: 10.1016/0012-821X(95)00104-K.

Harigane, Y., Michibayashi, K. & Ohara Y. (2011). Deformation and hydrothermal metamorphism of gabbroic rocks within the Godzilla Megamullion, Parece Vela Basinm Philippine Sea. *Lithos*, **124**, 185-199, doi: 10.1016/j.lithos.2011.02.001.

Hébert, R., Serri, G. & Hekinian, R. (1989). Mineral chemistry of ultramafic tectonites and ultramafic to gabbroic cumulates from the major oceanic basins and Northern Apennines ophiolites (Italy) – a comparison. *Chemical Geology*, **77**, 183-207, doi: 10.1016/0009-2541(89)90074-0.

Higgie, K. & Tommasi, A. (2012). Feedbacks between deformation and melt distribution in the crust-mantle transition zone of the Oman ophiolite. *Earth and Planetary Science Letters*, **359-360**, 61-72, doi: 10.1016/j.epsl.2012.10.003.

Higgie, K. & Tommasi, A. (2014). Deformation in a partially molten mantle: Constraints from plagioclase lherzolites from Lanzo, western Alps. *Tectonophysics*, **615-616**, 167-181, doi: 10.1016/j.tecto.2014.01.007.

Hoogerduijn-Strating, E. H., Piccardo, G. B., Rampone, E., Scambelluri, M. & Vissers, R. L. (1990). The structure and petrology of the Erro-Tobbio peridotite, Voltri massif, Ligurian Alps:

Guidebook for a two-day-excursion with emphasis on processes in the upper mantle. *Ofioliti*, **15**, 119–184.

Hoogerduijn Strating, E. H., Rampone, E., Piccardo, G. B., Drury, M. R. & Vissers, R. L. M. (1993). Subsolidus emplacement of mantle peridotites during incipient oceanic rifting and opening of the Mesozoic Tethys (Voltri Massif, NW Italy). *Journal of Petrology,* **34**, 901-927, doi: 10.1093/petrology/34.5.901.

Husen, A., Renat, R. A. & Holtz, F. (2016). The effect of H2O and Pressure on Multiple Saturation and Liquid Lines of Descent in Basalt from the Shatsky Rise. *Journal of Petrology*, **57**, 309-344, doi: 10.1093/petrology/egw008.

Jousselin, D., Nicolas, A. & Boudier, F. (1998). Detailed mapping of a mantle diapir below a paleo-spreading center in the Oman ophiolite. *Journal of Geophysical Research,* **103**, 18153-18170, doi:10.1029/98JB01493.

Jousselin, D., Morales, L. F. G., Nicolle, M. & Stephant, A. (2012). Gabbro layering induced by simple shear in the Oman ophiolite Moho Transition Zone. *Earth and Planetary Science Letters,* **331-332**, 55-66, doi: 10.1016/j.epsl.2012.02.022.

Karato, S. I., Jung, H., Katamaya, I. & Skemer, P. (2008). Geodynamic significance of seismic anisotropy of the upper mantle: New insights from laboratory studies. *Annual Review of Earth and Planetary Sciences,* **36**, 59-93, doi: 10.1146/annurev.earth.36.031207.124120.

Kelemen, P. B., Hitehead, J. A., Aharonov, E. & Jordahl, K. A. (1995a). Experiments on flow focussing in soluble porous media, with applications to melt extraction from the mantle. *Journal of Geophysical Res*earch, **100**, 475-496, doi: 10.1029/94JB02544.

Kelemen, P. B., Shimizu, N. & Salters, V. J. M. (1995b). Extraction of mid-ocean-ridge basalt from the upwelling mantle by focused flow of melt in dunite channels. *Nature,* **375**, 747–753, doi: 10.1038/375747a0.

Kelemen, P. B., Braun, M. & Hirth, G. (2000). Spatial distribution of melt conduits in the mantle beneath oceanic spreading ridges: Observations from the Ingalls and Oman ophiolites. *Geochemistry, Geophysics, Geosystems,* **1**, 1999GC000012.

Kelemen, P. B., Kikawa, E., Miller, D. J. and Shipboard Scientific Party (2007). Leg 209 summary: processes in a 20-km thick conductive boundary layer beneath the Mid-Atlantic Ridge, 14°–16°N. In Kelemen, P.B., Kikawa, E., and Miller, D.J. (Eds.), *Proceedings of the Ocean Drilling Project, Scientific Results,* **209**, 1–33, College Station, TX (Ocean Drilling Program), doi: 10.2973/odp.proc.sr.209.001.2007.

Kinzler, R. J. & Grove, T. L. (1993). Corrections and further discussion of the primary magmas of mid-ocean ridge basalts, 1 and 2. *Journal of Geophysical Research*, **98**, 22339-22347, doi: 10.1029/93/JB02164.

Klein, E. M. & Langmuir, C. H. (1987). Global correlations of ocean ridge basalt chemistry with axial depth and crustal thickness. *Journal of Geophysical Research*, **92**, 8089-8115, doi: 10.1029/JB092iB08p08089.

Lambart, S., Laporte, D. & Schiano, P. (2009). An experimental study of focused magma transport and basalt-peridotite interactions beneath mid-ocean ridges: implications for the generation of primitive MORB compositions. *Contributions to Mineralogy and Petrology*, **157**, 429-451, doi: 10.1007/s00410-008-0344-7.

Laubier, M., Grove, T. L. & Langmuir, C. H. (2014). Trace element mineral/melt partitioning for basaltic and basaltic andesitic melts: An experimental and laser ICP-MS study with application to the oxidation state of mantle source regions. *Earth and Planetary Science Letters*, **392**, 265-278, doi: 10.1016/j.epsl.2014.01.053.

Le Roux, V., Tommasi, A. & Vauchez, A. (2008). Feedback between melt percolation and deformation in an exhumed lithosphere-asthenosphere boundary. *Earth and Planetary Science Letters*, **274**, 401-413, doi: 10.1016/j.epsl.2008.07.053.

Liang, Y. (2003). Kinetics of crystal-melt reaction in partially molten silicates: 1. Grain scale processes. *Geochemistry, Geophysics, Geosystems*, **4**, doi: 10.1029/2002GC000375.

Liang, Y., Schiemenz, A., Hesse, M. A. & Parmentier, E. M. (2011). Waves, channels, and the preservation of chemical heterogeneities during melt migration in the mantle. *Geophysical Research Letters*, **38**, L20308, doi: 10.1029/2011GL049034.

Lissenberg, C. J. & Dick, H. J. B. (2008). Melt-rock reaction in the lower oceanic crust and its implications for the genesis of mid-ocean ridge basalt. *Earth and Planetary Science Letters*, **271**, 311-325, doi: 10.1016/j.epsl.2008.04.023.

Lissenberg, C. J., MacLeod, C. J., Howard, K. A. & Godard, M. (2013). Pervasive reactive melt migration through fast-spreading lower oceanic crust (Hess Deep, equatorial Pacific Ocean). *Earth and Planetary Science Letters,* **361**, 436-447, doi: 10.1016/j.epsl.2012.11.012.

Lissenberg, C. J. & MacLeod, C. J. (2016). A reactive porous flow control on Mid-Ocean Ridge magmatic evolution. *Journal of Petrology*, **57**, 2195-2220, doi: 10.1093/petrology/egw074.

Manatschal, G. & Müntener, O. (2009). A type sequence across an ancient magma-poor ocean-continent transition: the example of the western Alpine Tethys ophiolites. *Tectonophysics*, **73**, 4-19, doi: 10.1016/j.tecto.2008.07.021.

Marroni, M., Molli, G., Montanini, A. & Tribuzio, R. (1998). The association of continental crust rocks with ophiolites in the Northern Apennines (Italy): implications for the continent-ocean transition in the Western Tethys. *Tectonophysics*, **292**, 43-66, doi: 10.1016/S0040-1951(98)00060-2.

Miller, D. J., Abratis, M., Christie, D., Drouin, M., Godard, M., Ildefonse, B., Maeda, J., Weinsteiger, A., Yamasaki, T., Suzuki, Y., Niino, A., Sato, Y. & Takeda, F. (2009). Data report: microprobe analyses of primary mineral phases from Site U1309, Atlantis Massif, IODP Expedition 304/305. In: Blackman, D.K., Ildefonse, B., John, B.E., Ohara, Y., Miller, D.J., MacLeod, C.J., and the Expedition 304/305 Scientists, *Proceedings of the IODP*, **304/305**, College Station, TX (Integrated Ocean Drilling Program Management International Inc.), doi: 10.2204/iodp.proc.304305.202.2009.

Montanini, A., Tribuzio, R. & Vernia, L. (2008). Petrogenesis of basalts and gabbros from an ancient continent-ocean transition (External Ligurides ophiolites, Northern Italy). *Lithos*, **101**, 453-479, doi: 10.1016/j.lithos.2007.09.007.

Morgan, Z. & Liang, Y. (2005). An experimental study of the kinetics of lherzolite reactive dissolution with applications to melt channel formation. *Contributions to Mineralogy and Petrology*, **150**, 369-385, doi: 10.1007/s00410-005-0033-8.

Müntener, O. & Piccardo, G. B. (2003). Melt migration in ophiolitic peridotites: The message from Alpine-Apennine peridotites and implications for embryonic ocean basins. *Geological Society Special Publications*, **218**, 69–89, doi: 10.1144/GSL.SP.2003.218.01.05.

O'Driscoll, B., Donaldson, C. H., Troll, V. R., Jerram, D. A. & Emeleus, C. H. (2007). An origin for harrisitic and granular olivine in the Rum layered suite, NW Scotland: a crystal size distribution study. *Journal of Petrology*, **48**, 253-270, doi: 10.1093/petrology/eg1059.

Ottonello, G., Piccardo, G. B. & Ernst, W. G. (1979). Petrogenesis of some Ligurian peridotites – II rare earth element chemistry. *Geochimica et Cosmochimica Acta,* **43**, 1273-1284, doi: 10.1016/0016-7037(79)90118-2.

Paquet, M., Cannat, M., Brunelli, D., Hamelin, C. & Humler, E. (2016). Effect of melt/mantle interactions on MORB chemistry at the easternmost Southwest Indian Ridge (61°-67°E). *Geochemistry, Geophysics, Geosystems*, **17**, 4605-4640, doi: 10.1002/2016GC006385.

Piccardo, G. B., Rampone, E. & Vannucci, R. (1990). Upper mantle evolution during continental rifting and ocean formation: evidence from peridotites bodies of the Western Alpine-Northern Apennine system. *Membr. Soc. Geol. Fr.,* **156**, 323-333.

Piccardo, G. B., Rampone, E. & Vannucci, R. (1992). Ligurian peridotites and ophiolites: from rift to ocean formation in the Jurassic Ligure-Piemontese basin. *Acta Vulcanologica,* **2**, 313-325.

Piccardo, G. B., Müntener, O., Zanetti, A. & Pettke, T. (2004). Ophiolite peridotites of the Alpine-Apennine system: mantle processes and geodynamic relevance. *International Geological Review,* **40**, 1119-1159, doi: 10.2747/0020-6814.46.12.1119.

Piccardo G. B. & Vissers R. L. M. (2007). The pre-oceanic evolution of the Erro-Tobbio peridotite (Voltri Massif, Ligurian Alps, Italy). *Journal of Geodynamics*, **43**, 417–449, doi: 10.1016/j.jog.2006.11.001.

Piccardo, G. B., Zanetti, A. & Müntener, O. (2007). Melt/peridotite interaction in the Southern Lanzo peridotite: Field, textural and geochemical evidence. *Lithos*, **94**, 181-209, doi: 10.1016/j.lithos.2006.07.002.

Piccardo, G. B. & Guarnieri, L. (2010). Alpine peridotites from the Ligurian Tethys: an updated critical review. *International Geological Review* **52**, 1138–1159, doi: 10.1080/00206810903557829.

Pirard, C., Hermann, J. & O'Neill, H. St. C. (2013). Petrology and geochemistry of the Crust-Mantle boundary in a nascent arc, Massif du Sud ophiolite, New Caledonia, SW Pacific. *Journal of Petrology*, **54**, 1759-1792, doi: 10.1093/petrology/egt030.

Presnall, D. C. & Hoover, J. D. (1987). High pressure phase equilibrium constraints on the origin of mid-ocean ridge basalts, in: Mysen, B. O. (Ed.), Magmatic processes: Physicochemical principles, *Special publications - Geochemical Society*, **1**, 75-89.

Quick, J. E. (1981) Petrology and petrogenesis of the Trinity peridotite, an upper mantle diapir in the eastern Klamath mountains, northern California. *Journal of Geophysical Research*, **86**, 11837-11863, doi: 10.1029/JB086iB12p11837.

Quick, J. E. (1982) The origin and significance of large, tabular dunite bodies in the Trinity peridotite, Northern California. *Contributions to Mineralogy and Petrology*, **78**, 413-422, doi: 10.1007/BF00375203.

Rampone, E., Piccardo, G. B., Vannucci, R., Bottazzi P. & Ottolini, L. (1993). Subsolidus reactions monitored by trace element partitioning: the spinel- to plagioclase-facies transition in mantle peridotites. *Contributions to Mineralogy and Petrology*, **115**, 1–17, doi: 10.1007/BF00712974.

Rampone, E., Piccardo, G. B., Vannucci, R. & Bottazzi, P. (1997). Chemistry and origin of trapped melts in ophiolitic peridotites. *Geochimica et Cosmochimica Acta*, **61**, 4557-4569, doi: 10.1016/S0016-7037(97)00260-3.

Rampone, E., Hofmann, A. W. & Raczek, I. (1998). Isotopic contrasts within the Internal Liguride ophiolite (N-Italy): the lack of genetic mantle-crust link. *Earth and Planetary Science Letters*, **163**, 175-189, doi: 10.1016/S0012-821X(98)00185-X.

Rampone, E. & Piccardo, G. B. (2000). The ophiolite-oceanic lithosphere analogue: new insights from the Northern Apennine (Italy). *in* “Ophiolites and oceanic crust: new insights from field studies and Ocean Drilling Program”, Dilek, J., Moores, E., Elthon, D. & Nicolas, A. eds., *Geological Society of America*, Special Paper, **349**, 21-34, doi: 10.1130/0-8137-2349-3.21.

Rampone, E., Romairone, A. & Hofmann, A. W. (2004). Contrasting bulk and mineral chemistry in depleted peridotites: evidence for reactive porous flow. *Earth and Planetary Science Letters*, **218**, 491-506, doi: 10.1016/S0012-821X(03)00679-4.

Rampone, E., Romairone, A., Abouchami, W., Piccardo, G. B. & Hofmann, A. W. (2005). Chronology, petrology and isotope geochemistry of the Erro-Tobbio peridotites (Ligurian Alps, Italy): records of late Paleozoic lithospheric extension. *Journal of Petrology.* **46**, 799-827, doi: 10.1093/petrology/egi001.

Rampone, E. & Borghini, G. (2008). Melt migration and intrusion in the Erro-Tobbio peridotites (Ligurian Alps, Italy): Insights on magmatic processes in extending lithospheric mantle. *European Journal of Mineralogy*, **20**, 573-585, doi: 10.1127/0935-1221/2008/0020-1807.

Rampone, E., Piccardo, G. B. & Hofmann, A. W. (2008). Multi-stage melt-rock interaction in the Mt. Maggiore (Corsica, France) ophiolitic peridotites: microstructural and geochemical evidence. *Contributions to Mineralogy and Petrology*, doi: 10.1007/s00410-008-0296-y.

Rampone E., Borghini G., Romairone A., Abouchami W., Class C. & Goldstein S. L. (2014). Sm–Nd geochronology of the Erro-Tobbio gabbros (Ligurian Alps, Italy): Insights into the evolution of the Alpine Tethys. *Lithos*, **205**, 236-246, doi: 10.1016/j.lithos.2014.07.012.

Rampone, E., Borghini, G., Godard, M., Ildefonse, B., Crispini, L. & Fumagalli, P. (2016). Melt/rock reaction at oceanic peridotite/gabbro transition as revealed by trace element chemistry of olivine. *Geochimica et Cosmochimica Acta*, **190**, 309-331, doi: 10.1016/j.gca.2016.06.029.

Rampone, E., Borghini, G. & Basch, V. (2018). Melt migration and melt-rock reaction in the Alpine-Apennine peridotites: insights on mantle dynamics in extending lithosphere. *Geoscience Frontiers*, doi: .

Renna, M. R. & Tribuzio, R. (2011). Olivine-rich Troctolites from Ligurian Ophiolites (Italy): Evidence for Impregnation of Replacive Mantle Conduits by MORB-type Melts. *Journal of Petrology*, **52**, 1763-1790, doi: 10.1093/petrology/egr029.

Renna, M. R., Tribuzio, R. & Ottolini, L. (2016). New perspectives on the origin of olivine-rich troctolites and associated harrisites from the Ligurian ophiolites (Italy), *Journal of the Geological Society*, doi: 10.1144/jgs2015-135.

Rosenberg, C. L. & Handy, M. R. (2005). Experimental deformation of partially melted granite revisited: implications for the continental crust. *Journal of Metamorphic Geology*, **23**, 19-28, doi: 10.1111/j.1525-1314.2005.00555.x.

Ross, K. & Elthon, D. (1997). Cumulus and Postcumulus crystallization in the oceanic crust: major and trace elements geochemistry of Leg 153 gabbroic rocks. In: Karson, J.A., Cannat, M. and Miller, D.J. (eds.) *Proceedings of the Ocean Drilling Program, Scientific Results,* **143**, 333-350, College Station, TX, doi: 10.2973/odp.proc.sr.153.023.1997.

Saccani, E., Principi, G., Garfagnoli, F. & Menna, F. (2008) Corsica ophiolites: geochemistry and petrogenesis of basaltic and metabasaltic rocks. *Ofioliti*, **33**, 187-202.

Sanfilippo, A. & Tribuzio, R. (2012). Building of the deepest crust at a fossil slow-spreading centre (Pineto gabbroic sequence, Alpine Jurassic ophiolites). *Contributions to Mineralogy and Petrology*, **165**, 705-721, doi: 10.1007/s00410-012-0831-8.

Sanfilippo, A., Dick, H. J. B. & Ohara, Y. (2013). Melt-Rock reaction in the Mantle: Mantle troctolites from the Parece Vela Ancient Back-Arc Spreading Centre. *Journal of Petrology*, **54**, 61-885, doi: 10.1093/petrology/egs089.

Sanfilippo, A., Tribuzio, R. & Tiepolo, M. (2014). Mantle-crust interactions in the oceanic lithosphere: Constraints from minor and trace elements in olivine. *Geochimica et Cosmochimica Acta*, **141**, 423-439, doi: 10.1016/j.gca.2014.06.012.

Sanfilippo, A., Tribuzio, R., Tiepolo, M. & Berno, D. (2015a). Reactive flow as dominant evolution process in the lowermost oceanic crust: evidence from olivine of the Pineto ophiolite (Corsica). *Contributions to Mineralogy and Petrology*, **170**, 38, doi: 10.1007/s00410-015-1194-8.

Sanfilippo, A., Morishita, T., Kumagai, H., Nakamura, K., Okino, K., Hara, K., Tamura, A. & Arai, S. (2015b). Hybrid troctolites from mid-ocean ridges: inherited mantle in the lower crust. *Lithos*, **232**, 124-130, doi: 10.1016/j.lithos.2015.06.025.

Sanfilippo, A., Morishita, T. & Senda, R. (2016a). Rhenium-osmium isotope fractionation at the oceanic crust-mantle boundary. *Geology*, **44**, 167-170, doi: 10.1130/G37428.1.

Sanfilippo, A., Dick, H. J. B., Ohara, Y. & Tiepolo, M. (2016b). New insights on the origin of troctolites from the breakaway area of the Godzilla Megamullion (Parece Vela back-arc basin): The role of melt-mantle interaction on the composition of the lower crust. *Island arc*, **25**, 220-234, doi: 10.1111/iar.12137.

Sanfilippo, A., Tribuzio, R., Ottolini, L. & Hamada, M. (2017). Water, lithium and trace element compositions of olivine from Lanzo South replacive mantle dunites (Western Alps): New constraints into melt migration processes at cold thermal regimes. *Geochimica et Cosmochimica Acta*, **214**, 51-72, doi: 10.1016/j.gca.2017.07.034.

Saper, L. & Liang, Y. (2014). Formation of plagioclase-bearing peridotite and plagioclase-bearing wehrlite and gabbro suite through reactive crystallization: an experimental study. *Contributions to Mineralogy and Petrology*, **167**, 985, doi: 10.1007/s00410-014-0985-7.

Scambelluri, M., Hoogerduijn Strating, E. H., Piccardo, G. B., Vissers, R. L. M. & Rampone, E. (1991). Alpine olivine and titanian clinohumite bearing assemblages in the Erro-Tobbio peridotites. *Journal of Metamorphic Geology*, **9**, 79–91, doi: 10.1111/j.1525-1314.1991.tb00505.x.

Seyler, M., Cannat, M. & Mével, C. (2003). Evidence for major element heterogeneity in the mantle source of abyssal peridotites from the Southwest Indian Ridge (52° to 68°E). *Geochemistry, Geophysics, Geosystems*, doi: 10.1029/2002GC000305

Soustelle, V., Tommasi, A., Bodinier, J. L., Garrido, C. J. & Vauchez, A. (2009). Deformation and Reactive Melt Transport in the Mantle Lithosphere above a Large-scale Partial Melting Domain: The Ronda Peridotite Massif, Southern Spain. *Journal of Petrology*, **50**, 1235-1266, doi: 10.1093/petrology/egp032.

Soustelle, V., Tommasi, A., Demouchy, S. & Ionov, D. A. (2010). Deformation and fluid-rock interaction in the supra-subduction mantle: Microstructures and water contents in peridotite xenoliths from the Avacha Volcano, Kamchatka. *Journal of Petrology*, **51**, 363-394, doi: 10.1093/petrology/egp085.

Soustelle, V., Walte, N. P., Geeth, M. A., Manthilake, M. & Frost, D. J. (2014). Melt migration and melt-rock reactions in the deforming Earth's upper mantle: Experiments at high pressure and temperature. *Geology*, **42**, 83-86, doi: 10.1130/G34889.1.

Suhr, G., Hellebrand, E., Johnson, K. & Brunelli, D. (2008). Stacked gabbro units and intervening mantle: A detailed look at a section of IODP Leg 305, Hole U1309D. *Geochemistry, Geophysics, Geosystems*, **9**, Q10007, doi: 10.1029/2008GC002012.

Takazawa, E., Frey, F. A., Shimizu, N., Obata, M. & Bodinier, J-L. (1992) Geochemical evidence for melt migration and reaction in the upper mantle. *Nature*, **359**, 55-58, doi: 10.1038/359055a0.

Tommasi, A., Mainprice, D., Canova, G. & Chastel, Y. (2000). Viscoplastic self-consistent and equilibrium-based modeling of olivine lattice preferred orientations: Implications for the upper mantle seismic anisotropy. *Journal of Geophysical Research*, **105**, 7893-7908, doi: 10.1029/1999JB900411.

Tribuzio, R., Tiepolo, M., Vannucci, R. & Bottazzi, P. (1999). Trace element disribution within olivine-bearing gabbros from the Northern Apennine ophiolites (Italy): Evidence for post-cumulus crystallization in MOR-type gabbroic rocks. *Contributions to Mineralogy and Petrology*, **134**, 123-133, doi: 10.1007/s004100050473.

Tribuzio, R., Tiepolo, M. & Vannucci, R. (2000). Evolution of gabbroic rocks of the Northern Apennine ophiolites (Italy): Comparison with the lower oceanic crust from modern slow-spreading ridges, *in* Dilek, Y., Moores, E.M., Elthon, D., and Nicolas, A., eds., Ophiolites and Oceanic Crust: New Insights from Field Studies and the Ocean Drilling Program: Boulder, Colorado, *Geological Society of America*, **349**, 129–138, doi: 10.1130/0-8137-2349-3.129..

Tribuzio, R., Thirlwall, M. F. & Vanucci, R. (2004). Origin of the Gabbro-Peridotite association from the Northern Apennine Ophiolites (Italy). *Journal of Petrology*, **45**, 1109-1124, doi: 10.1093/petrology/egh006.

Tursack, E. & Liang, Y. (2012). A comparative study of melt-rock reactions in the mantle: laboratory dissolution experiments and geological field observations. *Contributions to Mineralogy and Petrology*, **163**, 861-876, doi: 10.1007/s00410-011-0703-7.

Van den Bleeken, G., Müntener, O. & Ulmer, P. (2011). Melt variability in percolated peridotite: an experimental study applied to reactive migration of tholeiitic basalt in the upper mantle. Contribution to Mineralogy and Petrology, **161**, 921-945, doi: 10.1007/s00410-010-0572-5.

Van der Wal, D. & Bodinier, J-L. (1996). Origin of the recrystallization front in the Ronda peridotite by km-scale pervasive porous melt flow. *Contributions to Mineralogy and Petrology*, **122**, 387-405, doi: 10.1007/s004100050.

Vissers R. L. M., Drury M. R., Hoogerduijn Strating E. H. & Van der Wal D. (1991). Shear zones in the upper mantle: a case study in an Alpine lherzolite massif. *Geology*, **19**, 990-993, doi: 10.1130/0091-7613(1991)019<0990:SZITUM>2.3.CO;2.

Figure captions:

Figure 1: A: Sketch map of the Northern Apennines and Western Alps (redrawn after Piccardo & Vissers, 2007). The red square indicates the location of the Voltri Massif, in the Ligurian Alps; B: Map of the Voltri Massif and location of the studied area within the Erro Tobbio peridotites (redrawn after Piccardo & Vissers, 2007); C: Geological map of the Mt.Foscallo area, in the Erro-Tobbio peridotites. This structural map merges new data measured on the field with previously published data from Borghini *et al.*, 2007 and Borghini & Rampone, 2007.

Figure 2: Troctolite A field structures. A: Troctolite apophysis within the mantle peridotites at the contact between the troctolitic body and the peridotites (“transition zone”), and gabbroic dike crosscutting the association between peridotites and troctolites. B: Plagioclase-rich layering within the host Troctolite A; C: Crosscutting relationship between Troctolite A and Troctolite B; D: Dunitic pod included within the Troctolite A.

Figure 3: Troctolite B field structures. A: Troctolite B crosscutting the layering of plagioclase enrichment in Troctolite A (red dashed lines); B: Irregular contact between Troctolite A and crosscutting Troctolite B; C: Textural complexity within the Troctolite B; The white square indicates the location of (d); D: Dendritic “fishbone” olivine crystal; E: Textural variability of olivine crystals at centimetre-scale within the Troctolite B; The dashed red line separates granular olivine domains from hopper and dendritic olivine domains.

Figure 4: Representative sketch of the crosscutting relationships observed in the field among the impregnated peridotites, the composite troctolitic body, and the gabbroic intrusions.

Figure 5: Textural variability in the Troctolite A. A: Granular olivine matrix embedded in undeformed poikilitic plagioclase; B: Granular olivine matrix embedded in poikilitic clinopyroxene. The largest olivine crystal shows the occurrence of kink bands, highlighted by the red dashed lines. Interstitial plagioclase has been replaced by low-grade alteration phases; C: Corroded olivine grain prior to disruption into several smaller crystals. Interstitial plagioclase has been replaced by low-

grade alteration phases; D: Highly corroded centimetre-size olivine, embedded in poikilitic plagioclase.

Figure 6: EBSD phase (left column) and olivine misorientation (right column) maps showing the textural variability of the olivine matrix within the troctolitic body. A: Troctolite A with dunitic aggregates MF96B; B: Troctolite Apophysis MF51A1; C: Troctolite A with dunitic aggregates MF7A1; D: Troctolite A without dunitic aggregates MF102B1; E: Troctolite B MF101A. White areas in the phase maps are non-indexed pixels, mostly corresponding to altered plagioclase.

Figure 7: Textural variability observed into the Troctolite B pseudo-tabular bodies. Plagioclase is partly to completely replaced by low-grade alteration phases. A: Fine-grained granular undeformed olivines surrounded by a rim of chlorite; B: Partially corroded coarse hopper crystal of olivine, associated to poikilitic plagioclase and interstitial clinopyroxene; C: Coarse skeletal olivine showing the inner “branches” of olivine, associated to interstitial plagioclase and clinopyroxene; D: Single coarsed skeletal olivine associated to interstitial plagioclase.

Figure 8: Modal compositions and olivine Crystallographic Preferred Orientation of Spinel lherzolite, Plagioclase lherzolite, Troctolite apophysis, Troctolite A with and without olivine aggregates. One-point-per-grain equal-area, lower hemisphere stereographic projections. The colour bar is scaled to the maximum concentration of the three crystallographic axes. The foliation is indicated by the red line in oriented samples. J-index refers to the fabric strength.

Figure 9: Modal composition, olivine and plagioclase Crystallographic Preferred Orientation of Gabbroic intrusion and Troctolite B samples. One-point-per-grain equal-area, lower hemisphere stereographic projections. The colour bar is scaled to the maximum concentration of the three crystallographic axes. The foliation is indicated by the red line in oriented samples. J-index refers to the fabric strength.

Figure 10: A: Range of Forsterite content in olivines in Spinel Lherzolites, Plagioclase Lherzolite, Dunite, Troctolites A and Troctolites B; and B: Gabbroic intrusions. Olivine morphology is divided into Granular undeformed and Corroded deformed within the Troctolite A, and Granular undeformed and Hopper-Dendritic within the Troctolites B.

Figure 11: Major elements compositions of clinopyroxene cores (A-B) in all studied samples, plotted against the Mg-number = Mg/(Mg+Fe), and compositional variability with microstructural site (C, D) in Troctolites A. A-C: Cr_2O_3 (wt%); B-D: TiO_2 (wt%). Compositional fields represent compositions of olivine gabbros and troctolites from the South-West Indian Ridge, after Dick *et al.* (2002), Olivine-rich troctolites from the Erro-Tobbio, after Borghini & Rampone (2007), and Troctolites, olivine gabbros and gabbros from the Mid-Altantic Ridge Hole U1309D, after Suhr *et al.* (2008), Drouin *et al.* (2009); Miller *et al.* (2009) and Ferrando *et al.* (2018).

Figure 12: A-D: Reflected light photomicrographs and corresponding Clinopyroxene major element profile in Troctolite A. Step size is 19µm. B: Cr_2O_3 (wt%); C: TiO_2 (wt%); D: Al_2O_3 (wt%). Total length of the profile is 456µm. E-H: Reflected light photomicrographs and corresponding Plagioclase major element profile in Troctolite A. Step size is 54µm. F: Anorthite content (mol%); G: CaO (wt%); H: Al_2O_3 (wt%). Total length of the profile is 864µm. I-L: Reflected light photomicrographs and corresponding Olivine major element profile in Troctolite A. Step size is 10µm. J: Forsterite content (mol%); K: MgO (wt%); L: FeO (wt%). Total length of the profile is 600µm.

Figure 13: Range of Anorthite content in plagioclase in Troctolites A, Troctolites B and Gabbroic intrusions. Distinction has been made between cores (coloured symbols) and rims (white symbols) of coarse poikilitic plagioclase crystals.

Figure 14: A: Olivine – Clinopyroxene cores Mg# = Mg/(Mg+Fe) (mol%) correlation in the studied samples, compared to theoretical Fe-Mg equilibrium between olivine and clinopyroxenes, after Lissenberg & Dick (2008). The dashed lines represent the calculated olivine-clinopyroxene equilibrium line assuming an uncertainty of ±0.02 on the mineral-melt partition coefficients. B: Anorthite content (mol%) in plagioclase cores versus Forsterite content (mol%) in olivine cores in olivine-plagioclase couples from the studied Troctolites A, Troctolites B and Gabbroic intrusions. C: Anorthite content (mol%) in plagioclase cores versus Mg-number (mol%) in clinopyroxene cores in plagioclase-clinopyroxene couples from the studied Troctolites A, Troctolites B and Gabbroic intrusions. Compositional trends and fields represent olivine-plagioclase and olivine-clinopyroxene couples in olivine gabbros and troctolites from the South-West Indian Ridge (Hole735B: Dick *et al.*, 2002; 61-67°: Paquet *et al.*, 2016), the Mid-Atlantic Ridge Hole U1309D (Ross & Elthon, 1997; Lissenberg & Dick, 2008; Suhr *et al.*, 2008; Drouin *et al.*, 2009; Miller *et al.*, 2009), the Pineto

gabbroic crust (Sanfilippo & Tribuzio, 2012), and the Alpine-Apennine ophiolites (Hebert *et al.*, 1989; Tribuzio *et al.*, 1999; Montanini *et al.*, 2008; Sanfilippo & Tribuzio, 2012).

Figure 15: Interpretative sketch of the evolution of the olivine textures and associated CPOs during progressive olivine-dissolving, plagioclase-crystallizing melt-rock interaction and replacive formation of the Troctolite A. A: Coarse-grained dunite protolith showing an axial-[100] olivine CPO; B: Troctolite A impregnated at low melt-rock ratios, and thus preserving dunitic aggregates and axial-[100] olivine CPO; C: Disaggregated troctolite A, impregnated at high instantaneous melt-rock ratios. The arrows within small olivine grains represent the loss of cohesion of the solid matrix leading to the free rotation of the grains and randoming of the olivine CPO. CPO represented as one-point-per-grain equal-area, lower hemisphere stereographic projections. The colour bar is scaled to the maximum concentration of the three crystallographic axes. J-index refers to the fabric strength.

Figure 16: *pMELTs* numerical simulations (Ghiorso *et al.*, 2002) of the major element compositions of plagioclase (Anorthite content) vs A: olivine (Forsterite content), and B: clinopyroxene (Mg-value) during fractional crystallization and reactive crystallization of a sodic primitive MORB, after Saccani *et al.* (2008) (see text for detail). Varying assimilation rates of a dunite (100% olivine) from 1g/°C to 3g/°C of cooling are modelled, and compared to the core compositions of olivine-plagioclase, and clinopyroxene-plagioclase couples analyzed in the Troctolite A and Troctolite B. The green star represents the mineral compositions in equilibrium with the starting melt, and each dot along the crystal line of descent corresponds to a 5°C cooling step. The numbers along the fractional crystallization trend represent the remaining melt fraction at the saturation of plagioclase and clinopyroxene. Compositional fields of oceanic gabbroic suites are plotted as comparison for the South-West Indian Ridge (SWIR Hole 735B: Dick *et al.*, 2002; SWIR 61-67°E: Paquet *et al.*, 2016), the Mid-Atlantic Ridge (MAR; Ross & Elthon, 1997; Lissenberg & Dick, 2008; Suhr *et al.*, 2008; Drouin *et al.*, 2009; Miller *et al.*, 2009) and the Godzilla Megamullion (Godzilla MM; Harigane *et al.*, 2011; Sanfilippo *et al.*, 2013).

Figure 17: Representative sketch of the formation of Troctolite B. A: initial state, host Troctolite A crystal mush; B: prior crystallization of dendritic olivine by the undercooled melt; C: equilibrium crystallization of the fine-grained granular olivines.

Figure 18: *pMELTs* numerical modelling (Ghiorso *et al.*, 2002) of the major element compositions of olivine (Forsterite content), plagioclase (Anorthite content) and clinopyroxene (Mg-value) during

fractional crystallization of the melt modified after reactive equilibrium crystallization and formation of the Troctolite A and Troctolite B, compared to the major elements core compositions of olivine-plagioclase and clinopyroxene-plagioclase couples analyzed in the Erro-Tobbio Gabbroic intrusions. The green star represents the mineral compositions in equilibrium with the starting melt, and each dot along the crystal line of descent corresponds to a 5°C cooling step. Compositional fields of oceanic gabbroic suites similar to Figure 16.

Figure 19: Interpretative sketches of the geological context and evolution of the peridotitic and troctolitic body. A: Geological context of formation of the Erro-Tobbio troctolitic body at 175Ma, during the onset of the Ligurian Tethys basin rifting; B: Representative replacive formation of the Troctolite A from dunitic protolith, intrusion of the Troctolite B during focused melt percolation and intrusion of gabbroic rocks in fractures.

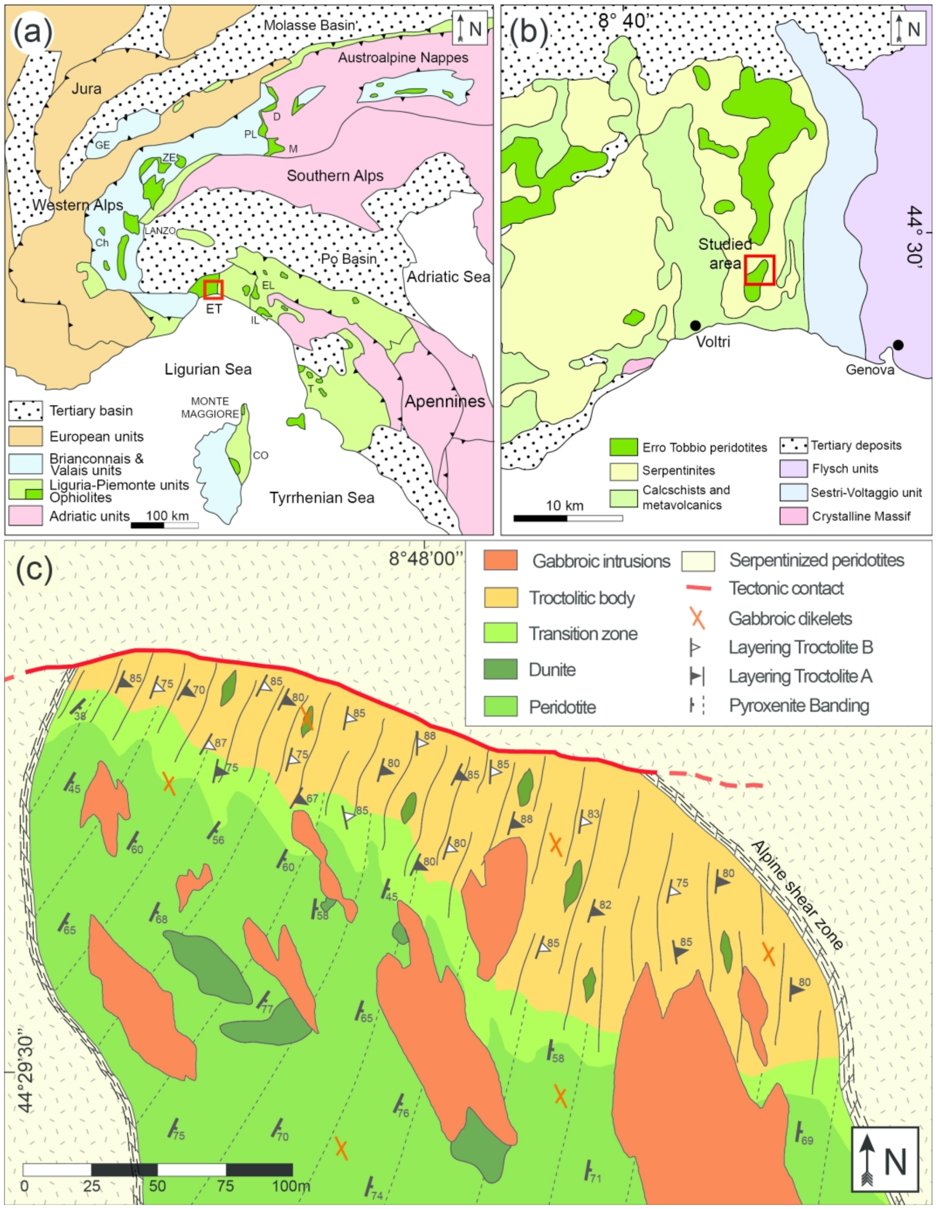

Figure 1: A: Sketch map of the Northern Apennines and Western Alps (redrawn after Piccardo & Vissers, 2007). The red square indicates the location of the Voltri Massif, in the Ligurian Alps; B: Map of the Voltri Massif and location of the studied area within the Erro Tobbio peridotites (redrawn after Piccardo & Vissers, 2007); C: Geological map of the Mt.Foscallo area, in the Erro-Tobbio peridotites. This structural map merges new data measured on the field with previously published data from Borghini et al., 2007 and Borghini & Rampone, 2007.

209x270mm (300 x 300 DPI)

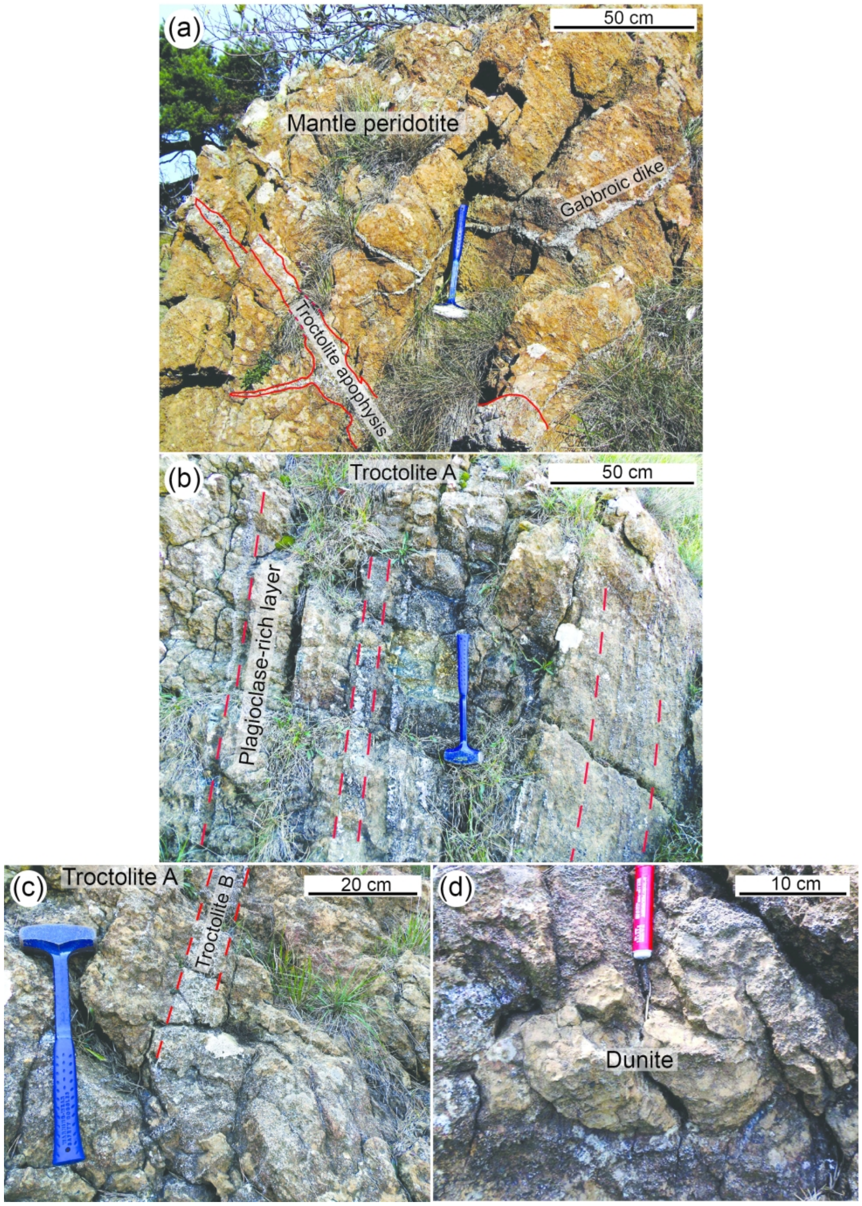

Figure 2: Troctolite A field structures. A: Troctolite apophysis within the mantle peridotites at the contact between the troctolitic body and the peridotites ("transition zone"), and gabbroic dike crosscutting the association between peridotites and troctolites. B: Plagioclase-rich layering within the host Troctolite A; C: Crosscutting relationship between Troctolite A and Troctolite B; D: Dunitic pod included within the Troctolite A.

209x293mm (300 x 300 DPI)

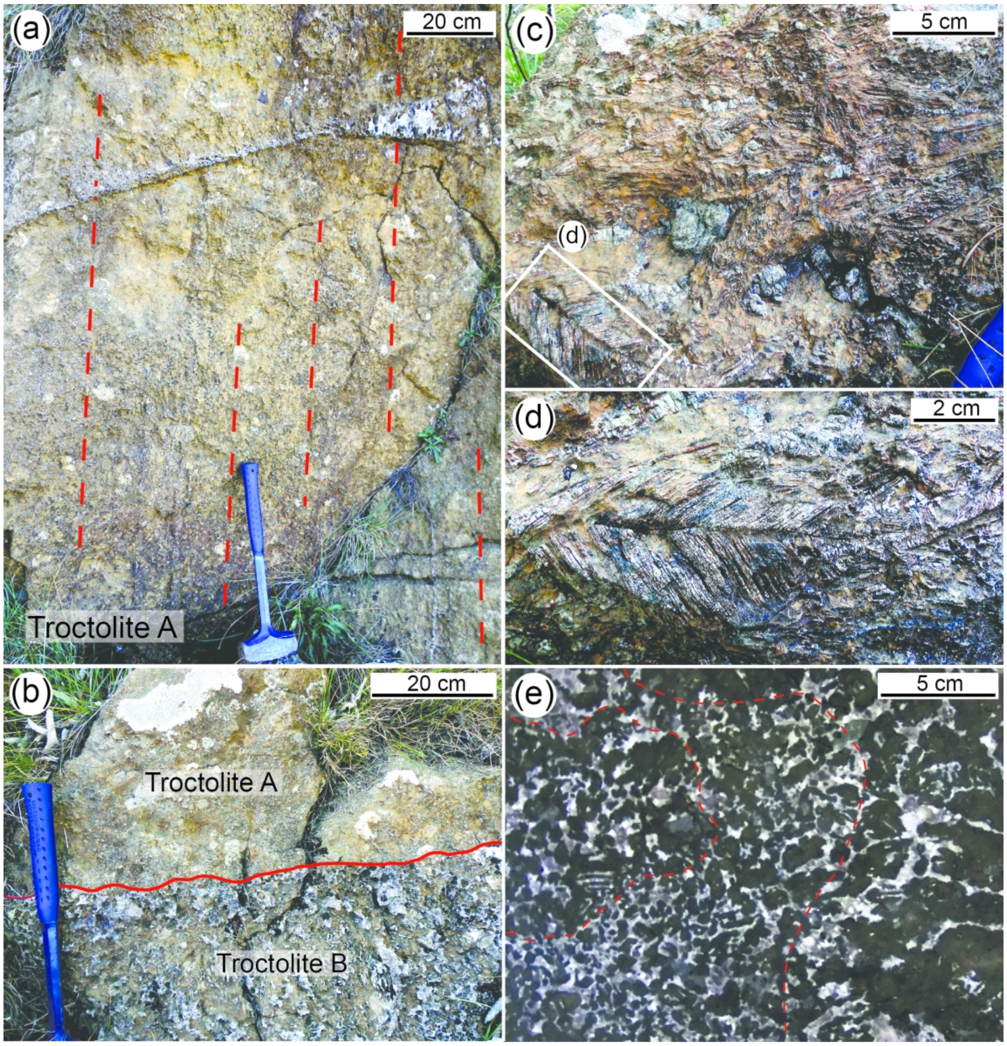

Figure 3: Troctolite B field structures. A: Troctolite B crosscutting the layering of plagioclase enrichment in Troctolite A (red dashed lines); B: Irregular contact between Troctolite A and crosscutting Troctolite B; C: Textural complexity within the Troctolite B; The white square indicates the location of (d); D: Dendritic "fishbone" olivine crystal; E: Textural variability of olivine crystals at centimetre-scale within the Troctolite B; The dashed red line separates granular olivine domains from hopper and dendritic olivine domains.

209x218mm (300 x 300 DPI)

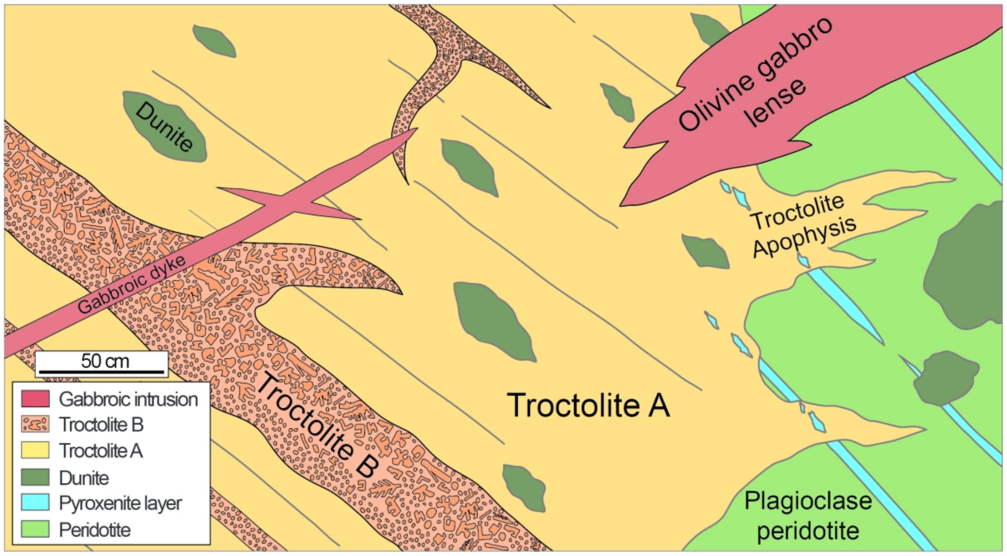

Figure 4: Representative sketch of the crosscutting relationships observed in the field among the impregnated peridotites, the composite troctolitic body, and the gabbroic intrusions.

210x115mm (300 x 300 DPI)

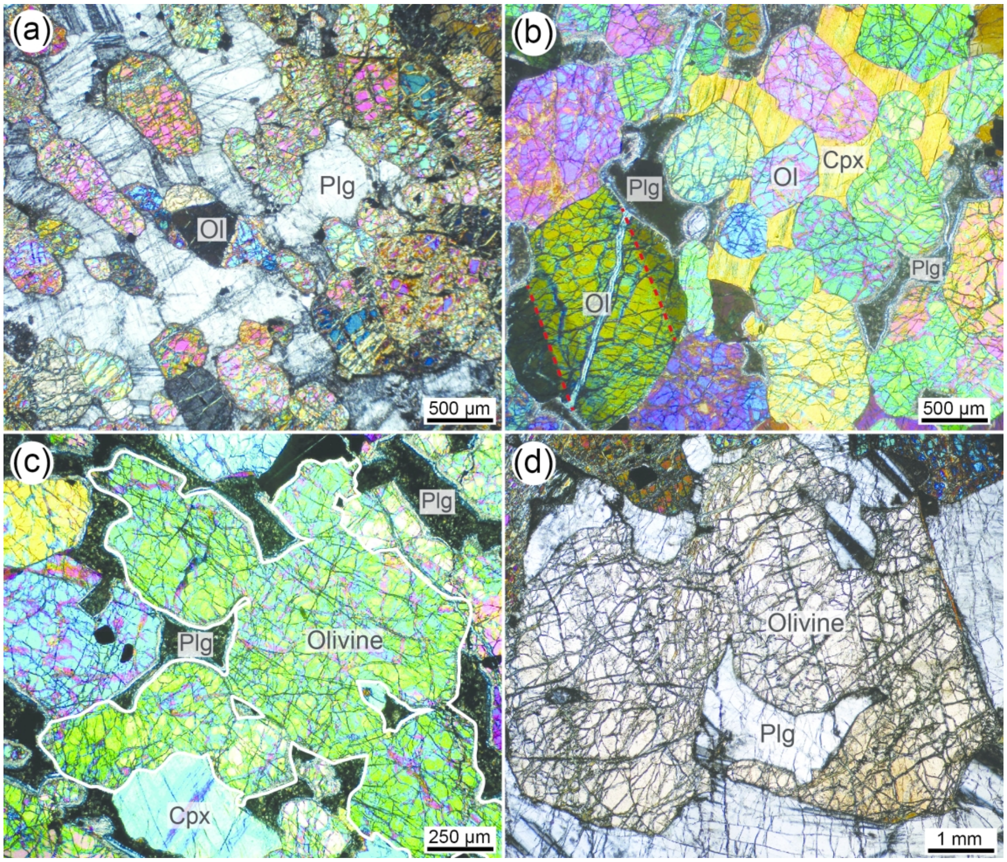

Figure 5: Textural variability in the Troctolite A. A: Granular olivine matrix embedded in undeformed poikilitic plagioclase; B: Granular olivine matrix embedded in poikilitic clinopyroxene. The largest olivine crystal shows the occurrence of kink bands, highlighted by the red dashed lines. Interstitial plagioclase has been replaced by low-grade alteration phases; C: Corroded olivine grain prior to disruption into several smaller crystals. Interstitial plagioclase has been replaced by low-grade alteration phases; D: Highly corroded centimetre-size olivine, embedded in poikilitic plagioclase.

209x179mm (300 x 300 DPI)

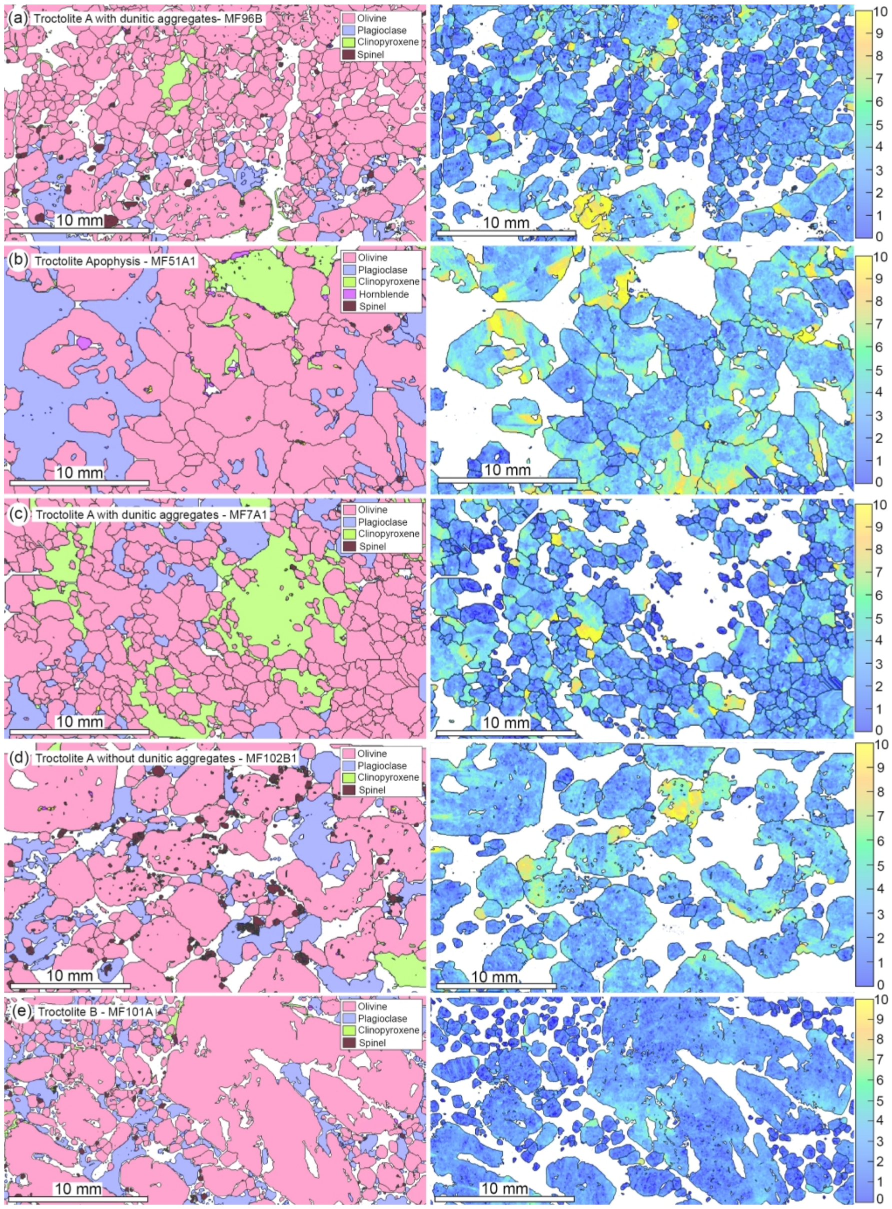

Figure 6: EBSD phase (left column) and olivine misorientation (right column) maps showing the textural variability of the olivine matrix within the troctolitic body. A: Troctolite A with dunitic aggregates MF96B; B: Troctolite Apophysis MF51A1; C: Troctolite A with dunitic aggregates MF7A1; D: Troctolite A without dunitic aggregates MF102B1; E: Troctolite B MF101A. White areas in the phase maps are non-indexed pixels, mostly corresponding to altered plagioclase.

209x284mm (300 x 300 DPI)

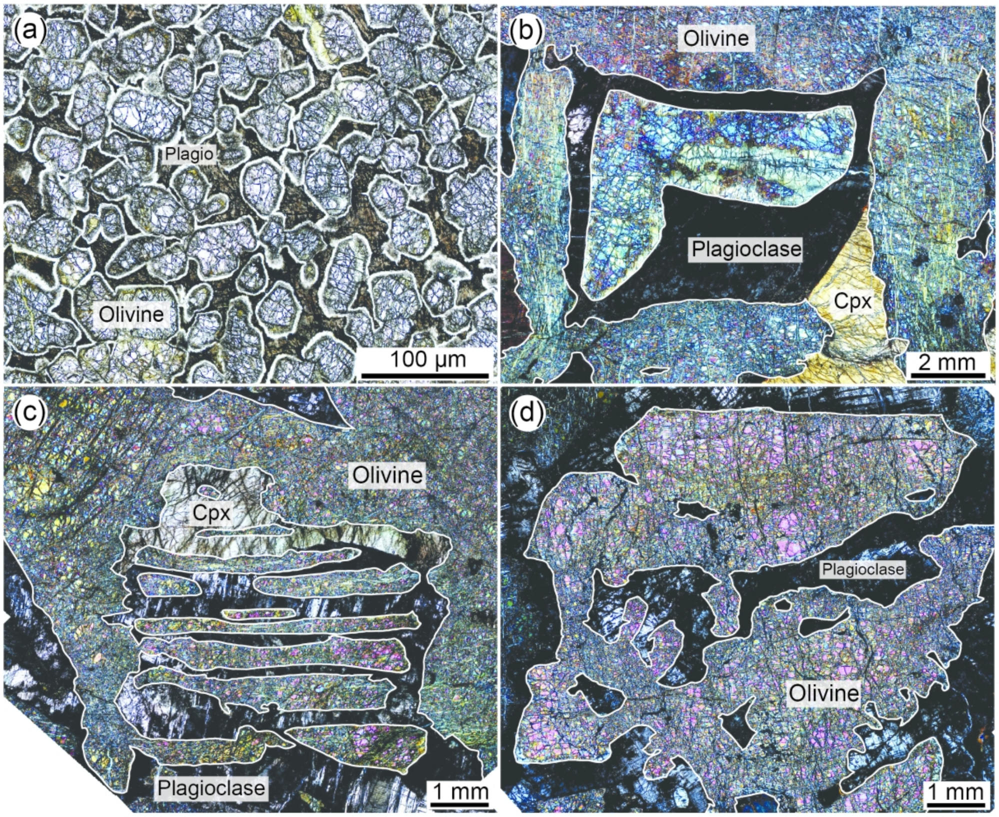

Figure 7: Textural variability observed into the Troctolite B pseudo-tabular bodies. Plagioclase is partly to completely replaced by low-grade alteration phases. A: Fine-grained granular undeformed olivines surrounded by a rim of chlorite; B: Partially corroded coarse hopper crystal of olivine, associated to poikilitic plagioclase and interstitial clinopyroxene; C: Coarse skeletal olivine showing the inner "branches" of olivine, associated to interstitial plagioclase and clinopyroxene; D: Single coarsed skeletal olivine associated to interstitial plagioclase.

212x173mm (300 x 300 DPI)

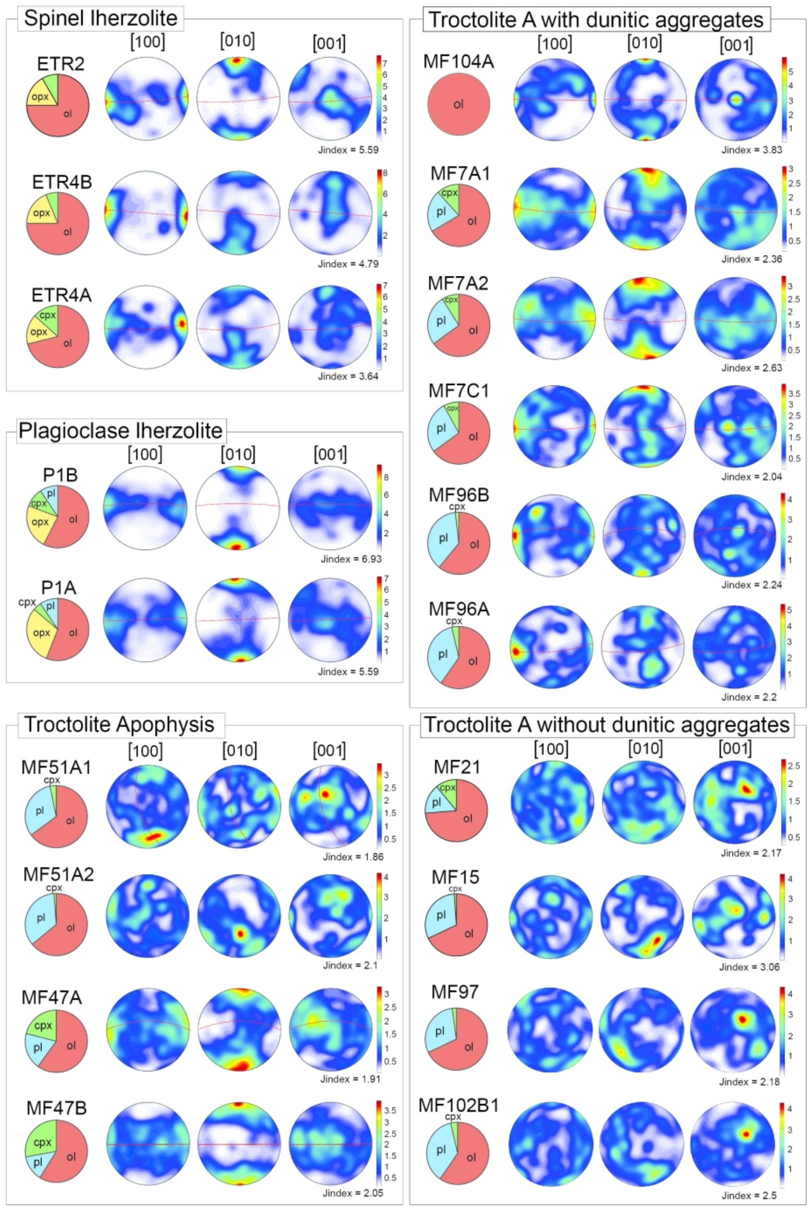

Figure 8: Modal compositions and olivine Crystallographic Preferred Orientation of Spinel lherzolite, Plagioclase lherzolite, Troctolite apophysis, Troctolite A with and without olivine aggregates. One-point-per-grain equal-area, lower hemisphere stereographic projections. The colour bar is scaled to the maximum concentration of the three crystallographic axes. The foliation is indicated by the red line in oriented samples. J-index refers to the fabric strength.

194x291mm (300 x 300 DPI)

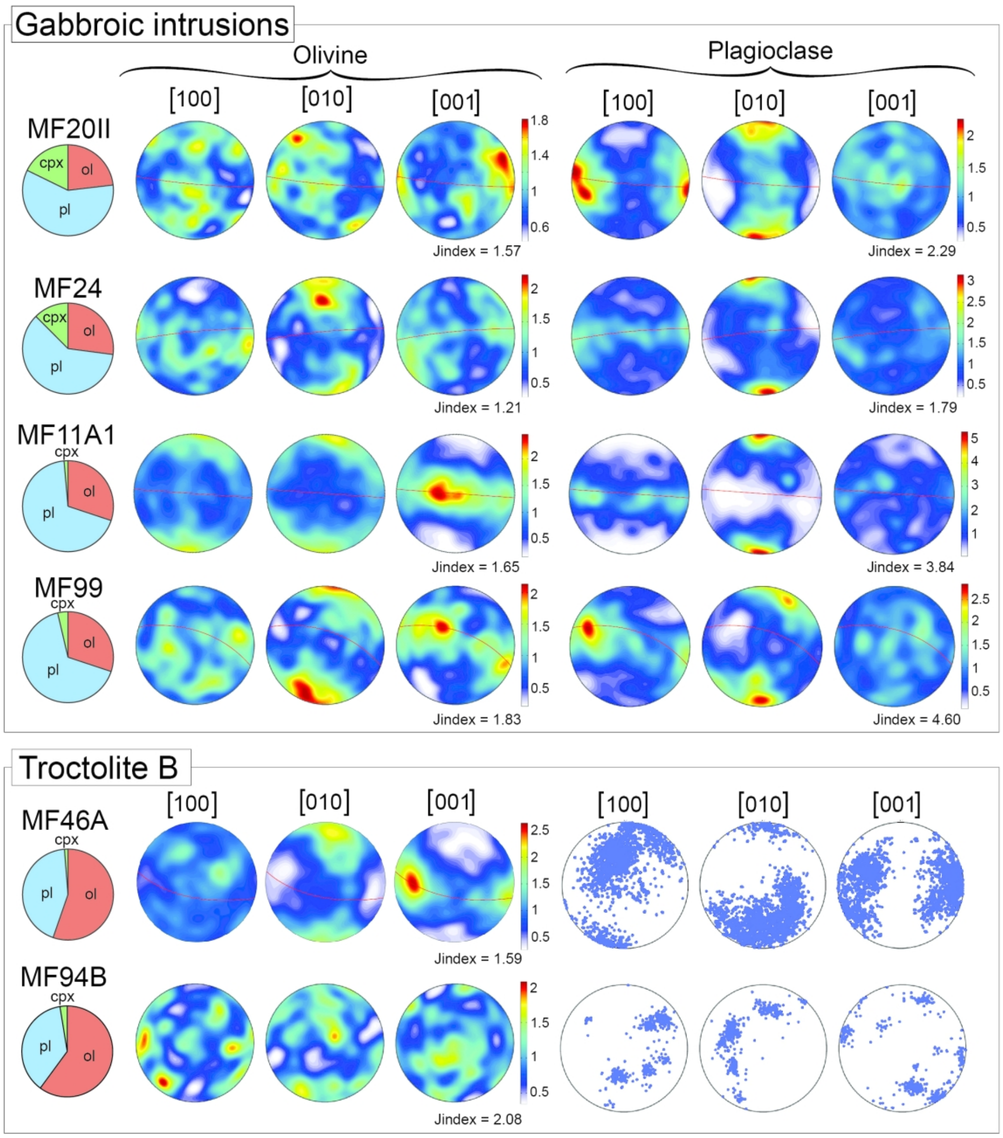

Figure 9: Modal composition, olivine and plagioclase Crystallographic Preferred Orientation of Gabbroic intrusion and Troctolite B samples. One-point-per-grain equal-area, lower hemisphere stereographic projections. The colour bar is scaled to the maximum concentration of the three crystallographic axes. The foliation is indicated by the red line in oriented samples. J-index refers to the fabric strength.

206x233mm (300 x 300 DPI)

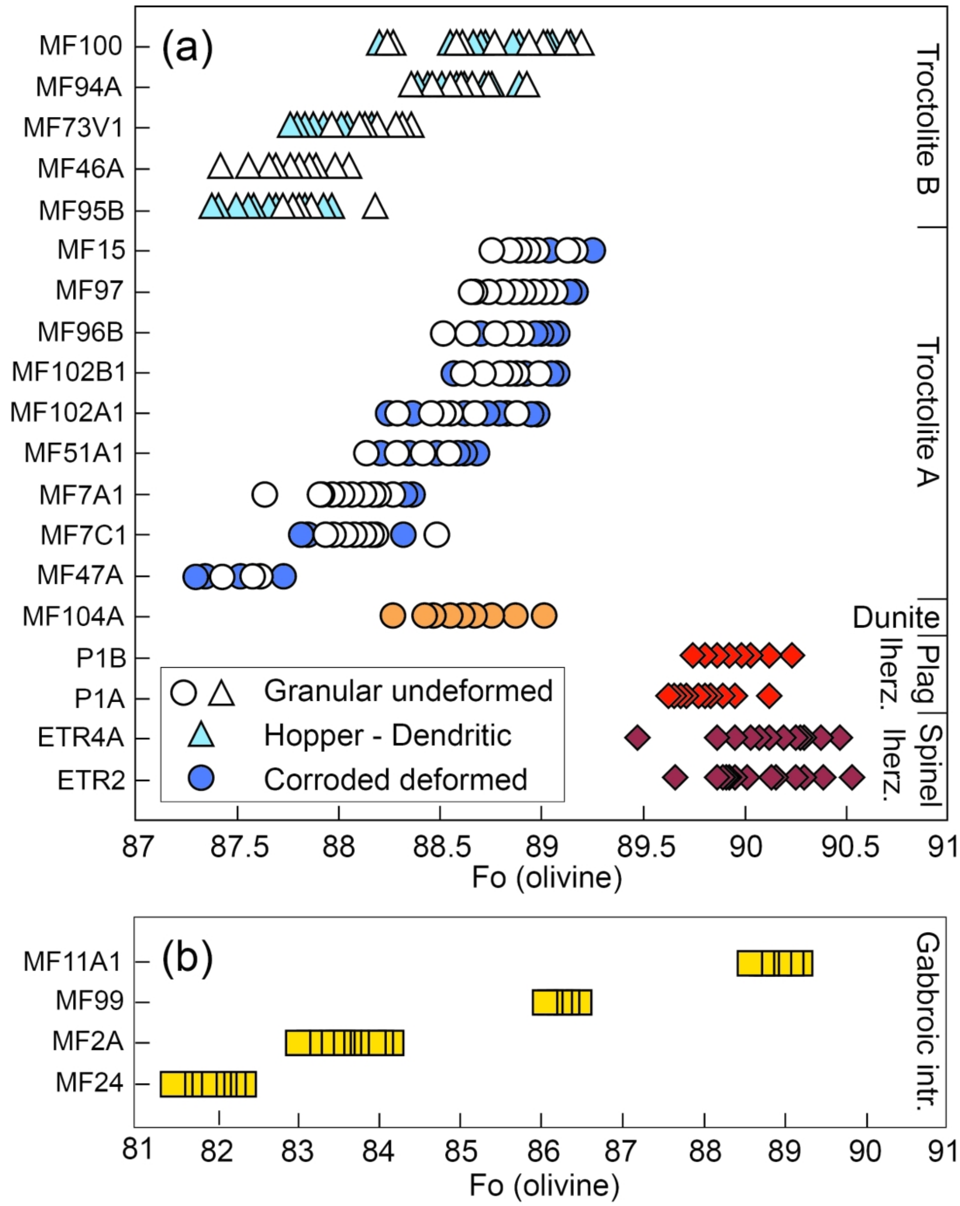

Figure 10: A: Range of Forsterite content in olivines in Spinel Lherzolites, Plagioclase Lherzolite, Dunite, Troctolites A and Troctolites B; and B: Gabbroic intrusions. Olivine morphology is divided into Granular undeformed and Corroded deformed within the Troctolite A, and Granular undeformed and Hopper-Dendritic within the Troctolites B.

186x235mm (300 x 300 DPI)

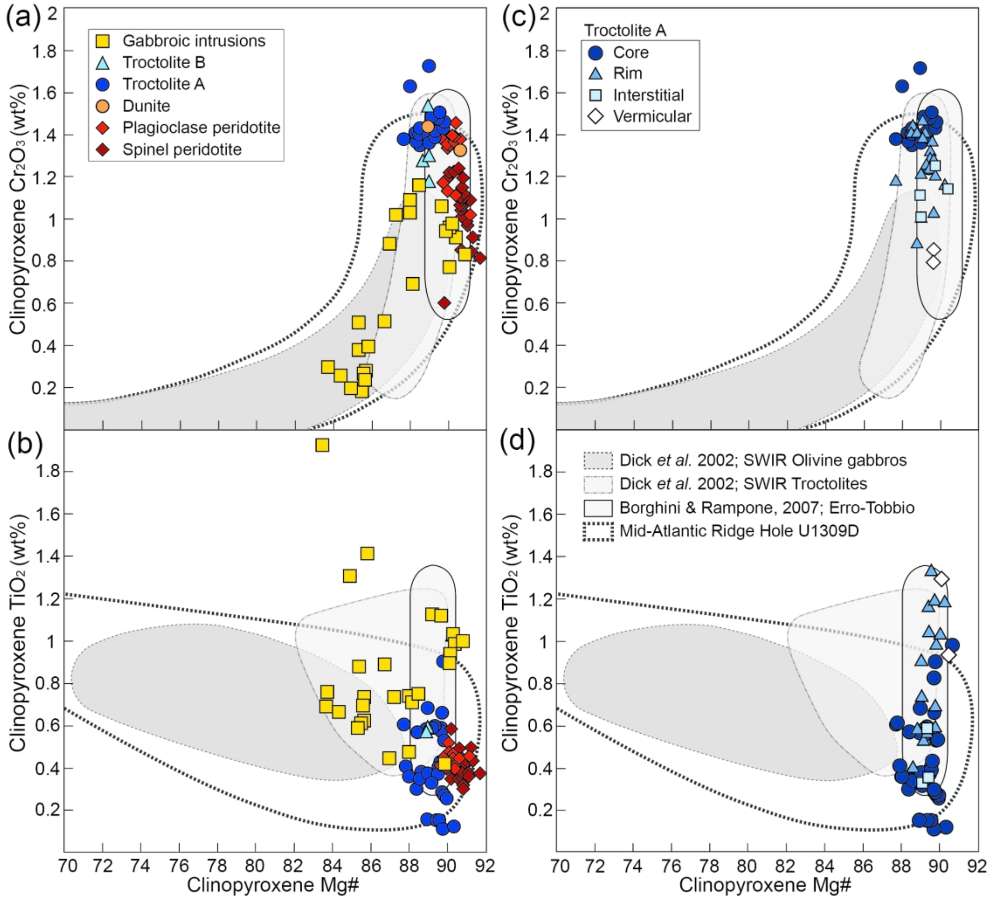

Figure 11: Major elements compositions of clinopyroxene cores (A-B) in all studied samples, plotted against the Mg-number = Mg/(Mg+Fe), and compositional variability with microstructural site (C, D) in Troctolites A. A-C: Cr2O3 (wt%); B-D: TiO2 (wt%). Compositional fields represent compositions of olivine gabbros and troctolites from the South-West Indian Ridge, after Dick et al. (2002), Olivine-rich troctolites from the Erro-Tobbio, after Borghini & Rampone (2007), and Troctolites, olivine gabbros and gabbros from the Mid-Altantic Ridge Hole U1309D, after Suhr et al. (2008), Drouin et al. (2009); Miller et al. (2009) and Ferrando et al. (2018).

212x193mm (300 x 300 DPI)

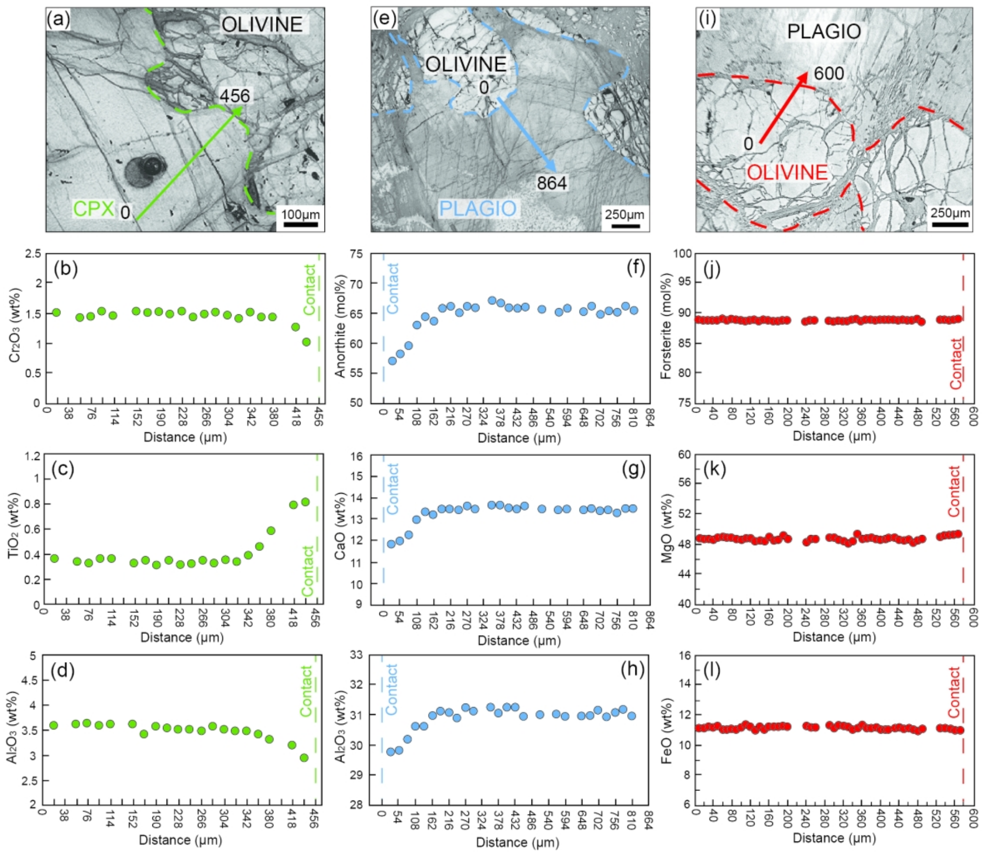

Figure 12: A-D: Reflected light photomicrographs and corresponding Clinopyroxene major element profile in Troctolite A. Step size is 19µm. B: Cr2O3 (wt%); C: TiO2 (wt%); D: Al2O3 (wt%). Total length of the profile is 456µm. E-H: Reflected light photomicrographs and corresponding Plagioclase major element profile in Troctolite A. Step size is 54µm. F: Anorthite content (mol%); G: CaO (wt%); H: Al2O3 (wt%). Total length of the profile is 864µm. I-L: Reflected light photomicrographs and corresponding Olivine major element profile in Troctolite A. Step size is 10µm. J: Forsterite content (mol%); K: MgO (wt%); L: FeO (wt%). Total length of the profile is 600µm.

210x181mm (300 x 300 DPI)

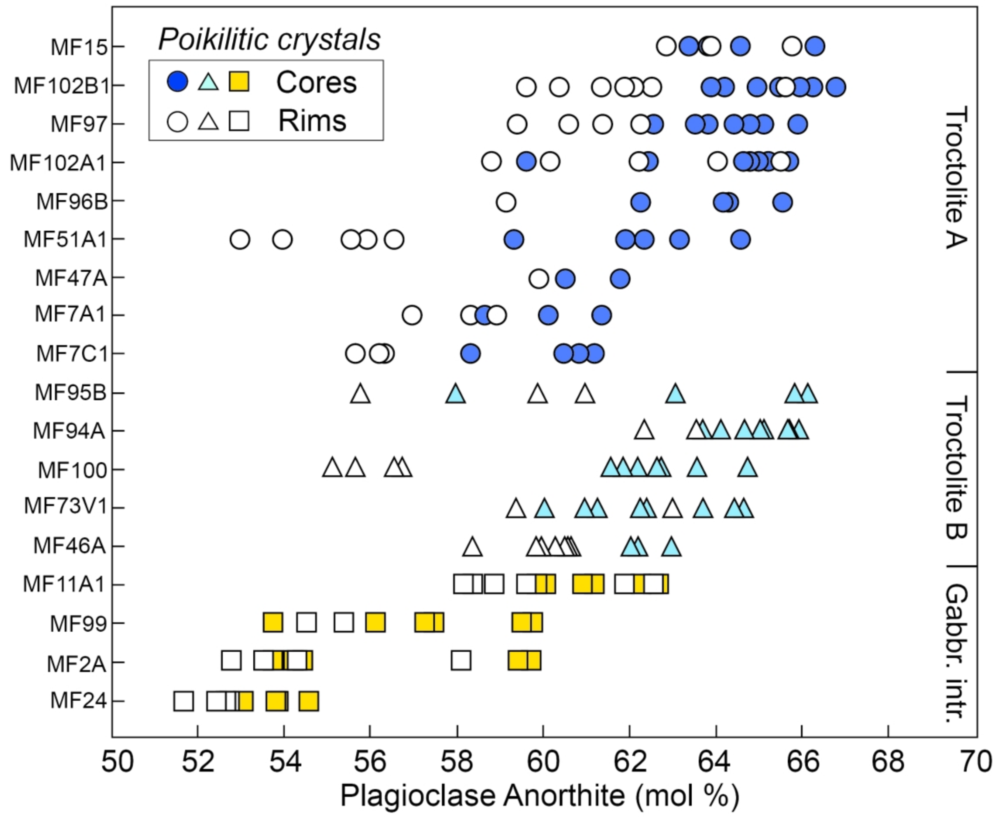

Figure 13: Range of Anorthite content in plagioclase in Troctolites A, Troctolites B and Gabbroic intrusions. Distinction has been made between cores (coloured symbols) and rims (white symbols) of coarse poikilitic plagioclase crystals.

218x182mm (300 x 300 DPI)

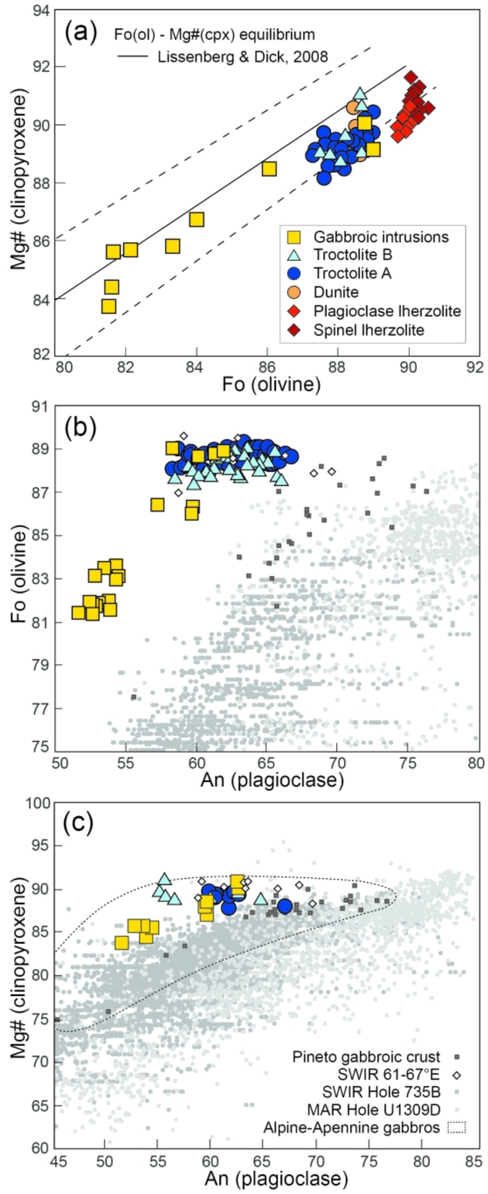

Figure 14: A: Olivine – Clinopyroxene cores Mg# = Mg/(Mg+Fe)(mol%) correlation in the studied samples, compared to theoretical Fe-Mg equilibrium between olivine and clinopyroxenes, after Lissenberg & Dick (2008). The dashed lines represent the calculated olivine-clinopyroxene equilibrium line assuming an uncertainty of ±0.02 on the mineral-melt partition coefficients. B: Anorthite content (mol%) in plagioclase cores versus Forsterite content (mol%) in olivine cores in olivine-plagioclase couples from the studied Troctolites A, Troctolites B and Gabbroic intrusions. C: Anorthite content (mol%) in plagioclase cores versus Mg-number (mol%) in clinopyroxene cores in plagioclase-clinopyroxene couples from the studied Troctolites A, Troctolites B and Gabbroic intrusions. Compositional trends and fields represent olivine-plagioclase and olivine-clinopyroxene couples in olivine gabbros and troctolites from the South-West Indian Ridge (Hole735B: Dick et al., 2002; 61-67°: Paquet et al., 2016), the Mid-Atlantic Ridge Hole U1309D (Ross & Elthon, 1997; Lissenberg & Dick, 2008; Suhr et al., 2008; Drouin et al., 2009; Miller et al., 2009), the Pineto gabbroic crust (Sanfilippo & Tribuzio, 2012), and the Alpine-Apennine ophiolites (Hebert et al., 1989; Tribuzio et al., 1999; Montanini et al., 2008; Sanfilippo & Tribuzio, 2012).

121x295mm (300 x 300 DPI)

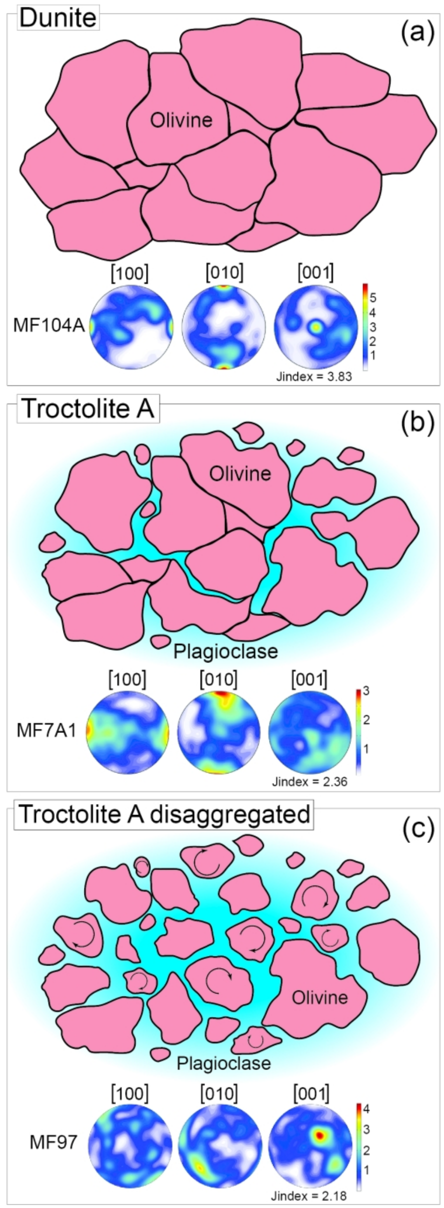

Figure 15: Interpretative sketch of the evolution of the olivine textures and associated CPOs during progressive olivine-dissolving, plagioclase-crystallizing melt-rock interaction and replacive formation of the Troctolite A. A: Coarse-grained dunite protolith showing an axial-[100] olivine CPO; B: Troctolite A impregnated at low melt-rock ratios, and thus preserving dunitic aggregates and axial-[100] olivine CPO; C: Disaggregated troctolite A, impregnated at high instantaneous melt-rock ratios. The arrows within small olivine grains represent the loss of cohesion of the solid matrix leading to the free rotation of the grains and randoming of the olivine CPO. CPO represented as one-point-per-grain equal-area, lower hemisphere stereographic projections. The colour bar is scaled to the maximum concentration of the three crystallographic axes. J-index refers to the fabric strength.

96x265mm (300 x 300 DPI)

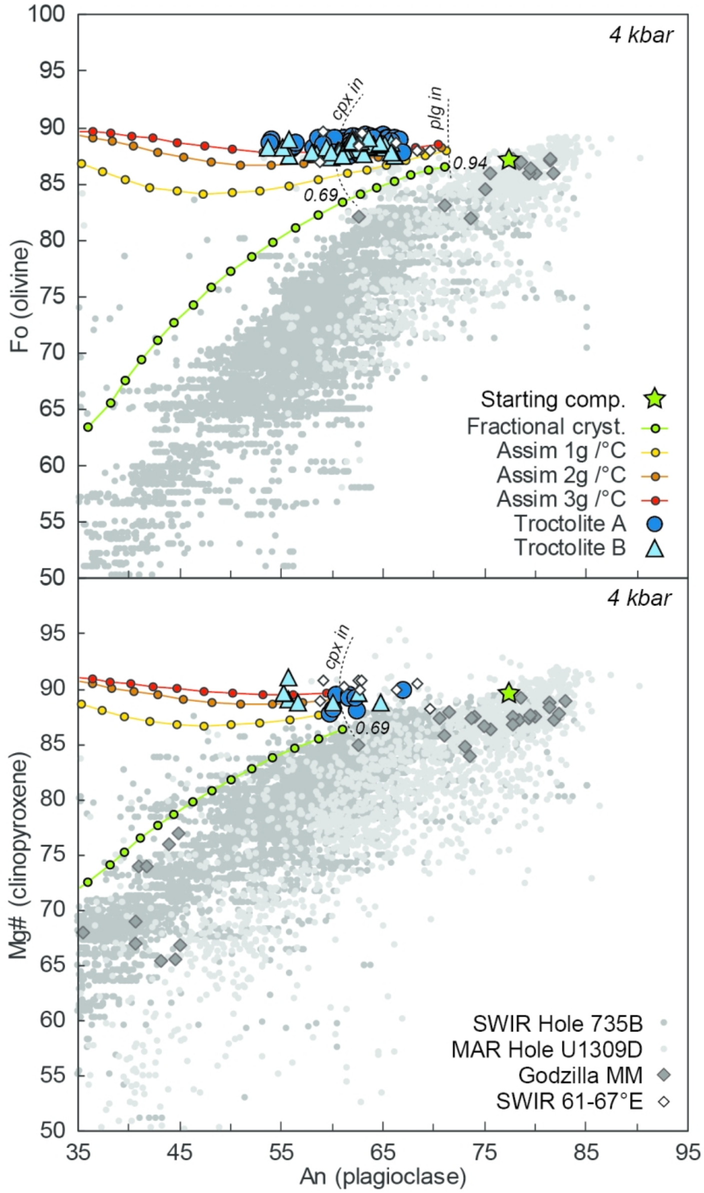

Figure 16: pMELTs numerical simulations (Ghiorso et al., 2002) of the major element compositions of plagioclase (Anorthite content) vs A: olivine (Forsterite content), and B: clinopyroxene (Mg-value) during fractional crystallization and reactive crystallization of a sodic primitive MORB, after Saccani et al. (2008) (see text for detail). Varying assimilation rates of a dunite (100% olivine) from 1g/°C to 3g/°C of cooling are modelled, and compared to the core compositions of olivine-plagioclase, and clinopyroxene-plagioclase couples analyzed in the Troctolite A and Troctolite B. The green star represents the mineral compositions in equilibrium with the starting melt, and each dot along the crystal line of descent corresponds to a 5°C cooling step. The numbers along the fractional crystallization trend represent the remaining melt fraction at the saturation of plagioclase and clinopyroxene. Compositional fields of oceanic gabbroic suites are plotted as comparison for the South-West Indian Ridge (SWIR Hole 735B: Dick et al., 2002; SWIR 61-67°E: Paquet et al., 2016), the Mid-Atlantic Ridge (MAR; Ross & Elthon, 1997; Lissenberg & Dick, 2008; Suhr et al., 2008; Drouin et al., 2009; Miller et al., 2009) and the Godzilla Megamullion (Godzilla MM; Harigane et al., 2011; Sanfilippo et al., 2013).

107x165mm (300 x 300 DPI)

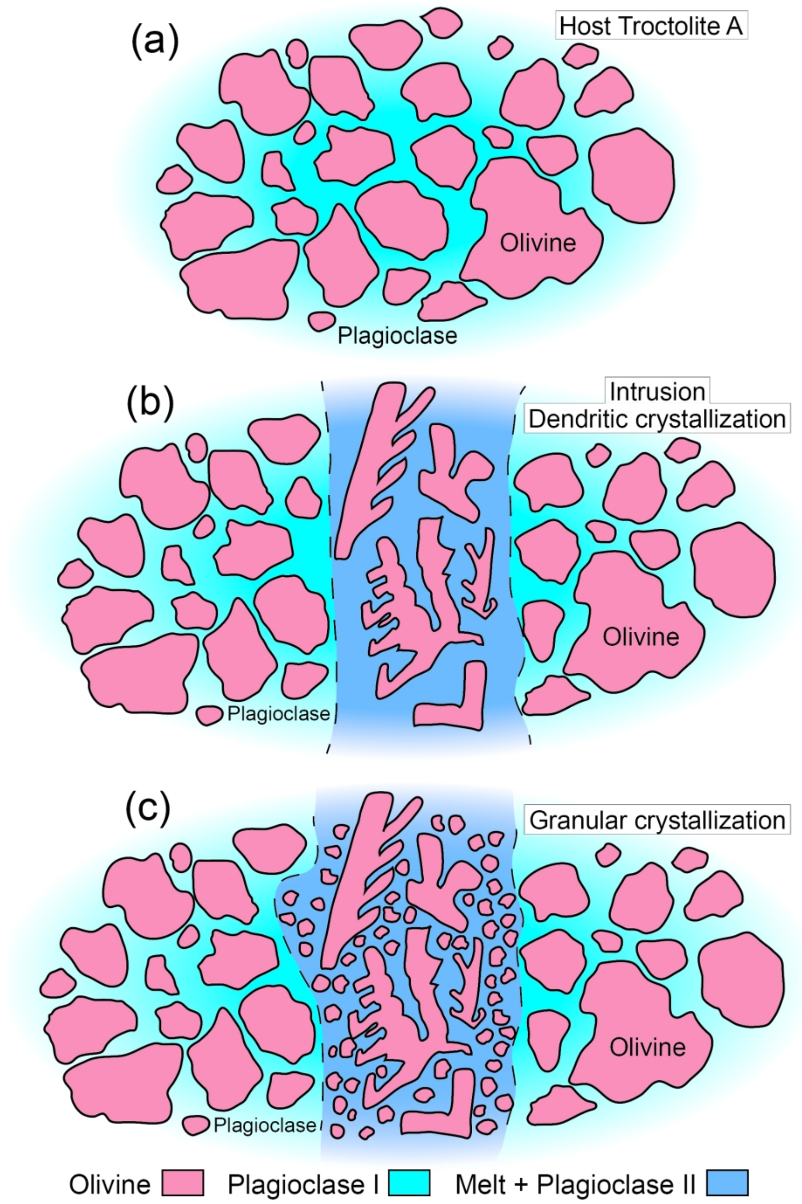

Figure 17: Representative sketch of the formation of Troctolite B. A: initial state, host Troctolite A crystal mush; B: prior crystallization of dendritic olivine by the undercooled melt; C: equilibrium crystallization of the fine-grained granular olivines.

167x250mm (300 x 300 DPI)

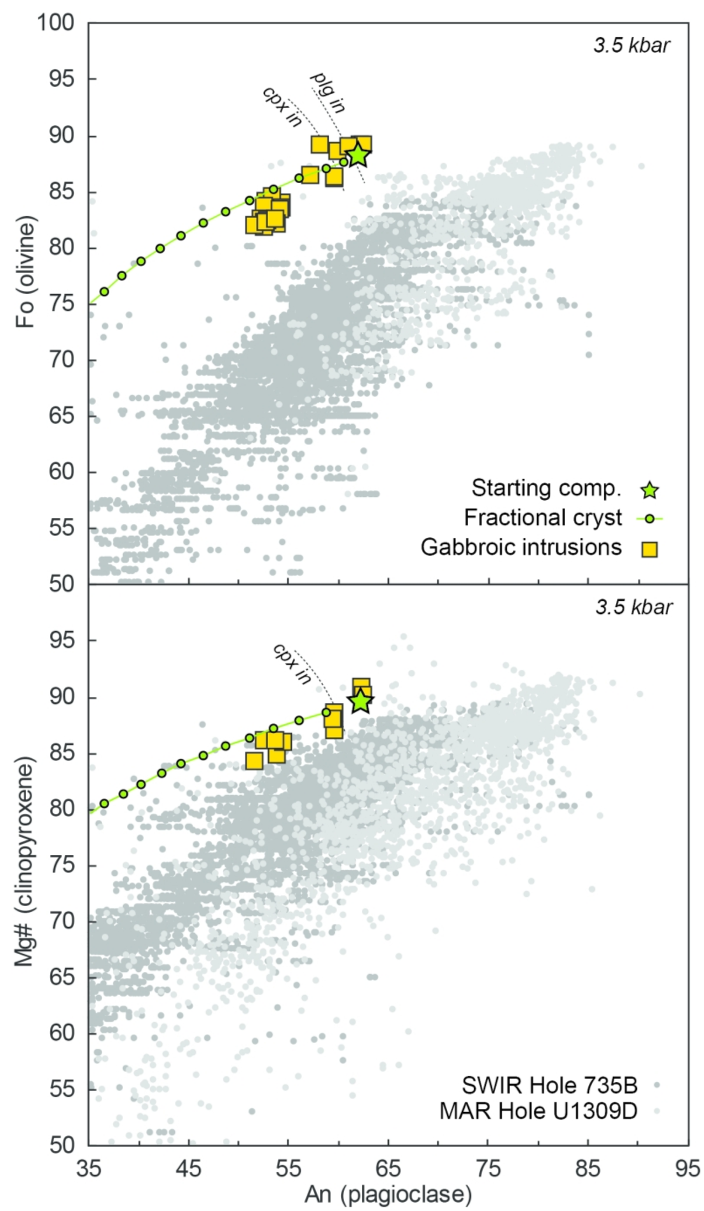

Figure 18: pMELTs numerical modelling (Ghiorso et al., 2002) of the major element compositions of olivine (Forsterite content), plagioclase (Anorthite content) and clinopyroxene (Mg-value) during fractional crystallization of the melt modified after reactive equilibrium crystallization and formation of the Troctolite A and Troctolite B, compared to the major elements core compositions of olivine-plagioclase and clinopyroxene-plagioclase couples analyzed in the Erro-Tobbio Gabbroic intrusions. The green star represents the mineral compositions in equilibrium with the starting melt, and each dot along the crystal line of descent corresponds to a 5°C cooling step. Compositional fields of oceanic gabbroic suites similar to Figure 16.

114x198mm (300 x 300 DPI)

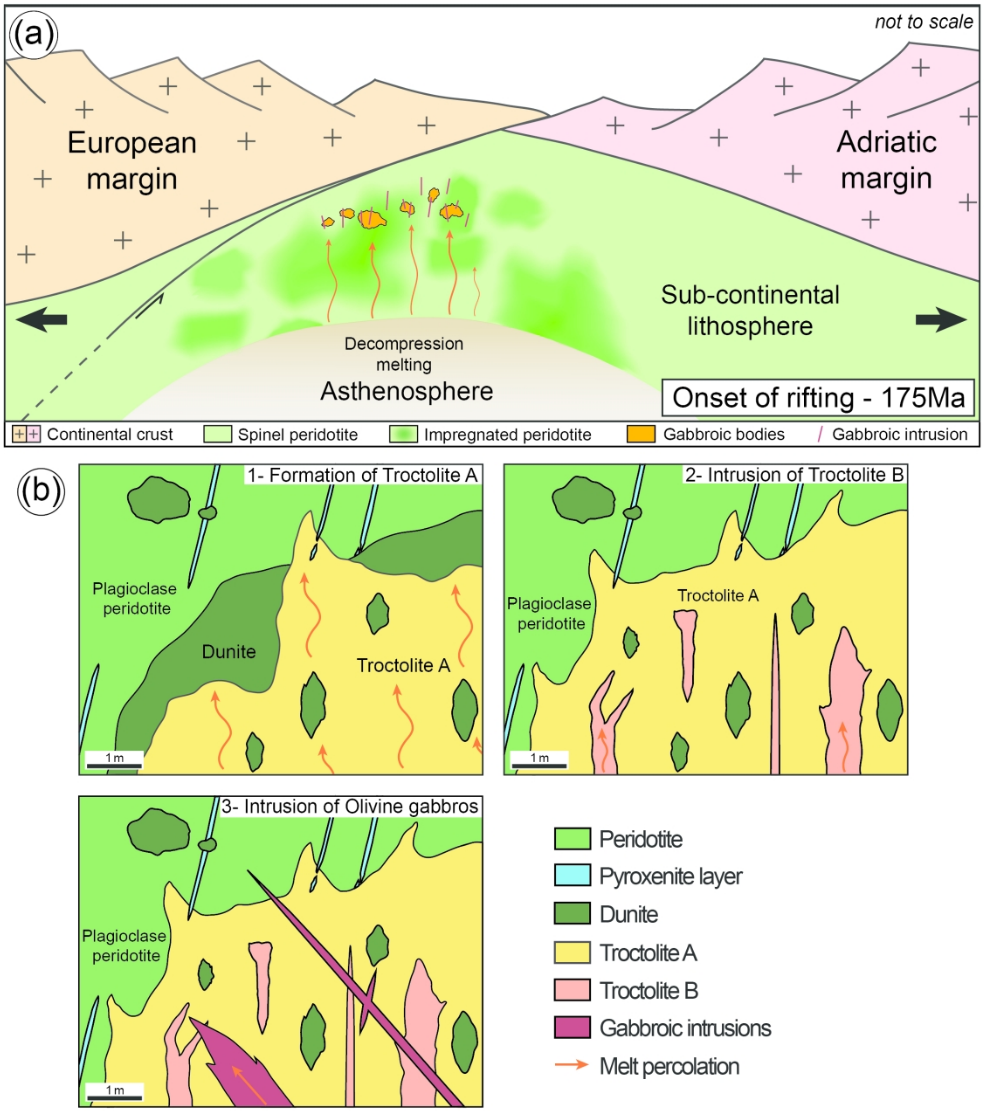

Figure 19: Interpretative sketches of the geological context and evolution of the peridotitic and troctolitic body. A: Geological context of formation of the Erro-Tobbio troctolitic body at 175Ma, during the onset of the Ligurian Tethys basin rifting; B: Representative replacive formation of the Troctolite A from dunitic protolith, intrusion of the Troctolite B during focused melt percolation and intrusion of gabbroic rocks in fractures.

210x237mm (300 x 300 DPI)

Table 1: Studied samples, lithotype, modal composition, and PfJ Olivine

		Modal compositions				PfJ Olivine		
Sample	Lithotype	Olivine	Plagio	Cpx	Opx	[100]	[010]	[001]
ETR2*	Spinel Lherzolite	78	0	7	15	2.33	2.84	2.02
ETR4B*	Spinel Lherzolite	75	0	5	20	2.24	1.64	1.56
ETR4A*	Spinel Lherzolite	71	0	14	15	2.08	1.65	1.32
P1B*	Plagio. Lherzolite	57	10	11	22	2.12	3.61	1.50
P1A*	Plagio. Lherzolite	56	10	4	30	1.90	2.67	1.40
P1*	Plagio. Lherzolite	55	12	11	22	2.53	4.17	2.23
MF40*	Plagio. Lherzolite	53	5	12	30	2.07	3.13	1.63
MF104A	Dunite	97	0	3	0	1.61	1.66	1.44
MF21*	Troctolite A	74	15	11	0	1.08	1.12	1.19
MF15*	Troctolite A	68	31	1	0	1.22	1.50	1.54
MF97	Troctolite A	68	30	2	0	1.19	1.33	1.4
MF51*	Troctolite Apophysis	67	32	1	0	1.77	1.68	1.88
MF7A1*	Troctolite A	66	23	11	0	1.52	1.58	1.23
MF7A2*	Troctolite A	65	26	9	0	1.39	1.77	1.21
MF7C1*	Troctolite A	65	27	8	0	1.24	1.40	1.12
MF51A1*	Troctolite Apophysis	65	32	3	0	1.37	1.24	1.39
MF51A2*	Troctolite Apophysis	64	35	1	0	1.25	1.48	1.41
MF96A	Troctolite A	60	39	1	0	1.14	1.28	1.17
MF96B	Troctolite A	61	37	2	0	1.25	1.18	1.13
MF102A1	Troctolite A	60	36	4	0	1.52	1.42	1.65
MF102B1	Troctolite A	60	36	4	0	1.19	1.34	1.42
MF47A*	Wehrlite Apophysis	60	19	21	0	1.16	1.44	1.17
MF47B*	Wehrlite Apophysis	59	13	28	0	1.22	1.47	1.14
MF102A2	Troctolite A	55	40	5	0	2.58	1.90	2.06
MF94B	Troctolite B	60	38	2	0	1.11	1.09	1.07
MF95A	Troctolite B	60	34	6	0	1.21	1.19	1.23
MF72Ga*	Troctolite B	59	31	10	0	1.41	1.31	1.37
MF95B	Troctolite B	59	36	5	0	1.37	1.28	1.36
MF72I*	Troctolite B	57	41	2	0	1.15	1.12	1.21
MF46A*	Troctolite B	55	44	1	0	1.04	1.23	1.3
MF73V2	Troctolite B	55	39	6	0			
MF94A	Troctolite B	55	42	3	0	2.50	1.85	1.85
MF73V1	Troctolite B	50	48	2	0	1.43	1.40	1.44
MF100	Troctolite B	45	51	4	0	1.64	1.88	1.71
MF11A1*	Troctolitic gabbro	30	69	1	0	1.08	1.10	1.3
MF99	Troctolitic gabbro	30	66	4	0	1.06	1.18	1.17
MF24*	Olivine gabbro	27	59	13	1	1.02	1.13	1.07
MF20*	Olivine gabbro	21	60	18	1	1.02	1.04	1.05
MF2B*	Olivine gabbro	16	63	19	2			
MF2A*	Olivine gabbro	15	68	16	1			

Plagio = Plagioclase; Cpx = Clinopyroxene; Opx = Orthopyroxene.
*samples investigated in previous studies (Rampone *et al.*, 2004, 2014, 2016; Borghini & Rampone, 2007; Borghini *et al.*, 2007; Rampone & Borghini, 2008). See text for further detail.

Table 2: Representative major elements olivine composition.

	Spinel Lherz.	Plagio. Lherz.	Dunite	Troctolite A		Troctolite apophysis		Wehrlite apophysis		Troctolite B		Troct. gabbro	Troct. gabbro	Olivine gabbro	Olivine gabbro
wt%	Corr.Def	Corr.Def	Corr.Def	Corr.Def	Granu.	Corr.Def	Granu.	Corr.Def	Granu.	Corr.Def.	Granu.	Granu.	Granu.	Granu.	Granu.
SiO_2	41.18	41.10	40.80	40.52	40.42	40.86	40.57	40.89	40.66	40.70	40.49	40.63	40.43	39.74	39.70
TiO_2	0.04	0.02	0.02	0.03	b.d.l.	b.d.l.	0.03	0.04	0.04	0.02	b.d.l.	0.01	b.d.l.	b.d.l.	0.03
Al_2O_3	0.01	b.d.l.	0.01	b.d.l.	0.02	b.d.l.	0.03	b.d.l.	b.d.l.	b.d.l.	0.04	b.d.l.	0.02	b.d.l.	b.d.l.
Cr_2O_3	b.d.l.	b.d.l.	0.02	b.d.l.	b.d.l.	b.d.l.	b.d.l.	0.01	b.d.l.	0.05	b.d.l.	b.d.l.	b.d.l.	b.d.l.	b.d.l.
FeO	9.64	10.05	11.29	11.65	11.75	11.31	11.29	11.81	11.96	11.61	11.52	11.11	13.38	16.11	17.57
MgO	49.47	48.99	47.65	48.05	48.02	48.01	48.21	47.33	47.33	47.90	48.05	48.22	46.49	44.35	43.16
MnO	0.11	0.16	0.21	0.18	0.15	0.23	0.15	0.20	0.22	0.18	0.17	0.17	0.21	0.27	0.33
NiO	0.37	0.43	0.28	0.30	0.28	0.33	0.29	0.27	0.31	0.31	0.32	0.33	0.26	0.21	0.14
CaO	0.03	0.06	0.09	0.06	0.04	0.07	0.05	0.05	0.04	0.08	0.02	0.04	0.01	b.d.l.	0.01
Total	100.85	100.83	100.37	100.81	100.69	100.84	100.63	100.60	100.58	100.86	100.63	100.54	100.80	100.68	100.96
Mg#	90.14	89.68	88.27	88.03	87.93	88.33	88.39	87.72	87.58	88.03	88.14	88.55	86.10	83.07	81.41

Mg# = Mg/(Mg+Fe); Spinel Lherz. = Spinel lherzolite; Plagio. Lherz. = Plagioclase lherzolite; Troct. Gabbro = Troctolitic gabbro

Table 3: Representative major elements clinopyroxene composition.

	Spinel Lherz.	Plagio. Lherz.		Dunite	Troctolite A		Troct. apophysis		Wehrlite apophysis	Troctolite B		Troct. gabbro	Troct. gabbro		Olivine gabbro	Olivine gabbro
wt%	Core	Core	Rim	Core	Core	Rim	Core	Rim	Core	Core	Rim	Core	Core	Rim	Core	Core
SiO_2	51.24	51.70	50.98	52.05	52.31	51.70	52.74	51.05	52.62	51.45	52.14	51.46	51.76	51.72	51.92	52.70
TiO_2	0.36	0.40	0.50	0.98	0.40	0.92	0.58	1.00	0.35	0.64	1.02	0.92	0.73	0.75	0.89	0.73
Al_2O_3	6.59	4.48	4.87	2.96	3.61	3.34	3.05	2.99	3.51	3.62	3.23	3.28	3.35	3.21	2.80	2.51
Cr_2O_3	1.10	1.46	1.34	1.32	1.43	1.16	1.08	1.00	1.29	1.40	0.91	0.94	1.01	1.15	0.51	0.28
FeO	2.83	3.01	3.20	3.08	3.45	3.22	3.43	3.37	3.42	3.57	3.17	3.23	4.33	3.76	4.63	5.15
MgO	15.23	15.81	16.05	16.64	16.51	16.32	16.68	17.61	16.09	15.94	16.32	16.49	16.56	16.21	16.93	17.25
MnO	0.07	0.02	0.07	0.12	0.07	0.08	0.18	0.07	0.10	0.11	0.09	0.10	0.15	0.17	0.27	0.16
NiO	0.07	0.06	0.07	0.02	b.d.l.	0.04	0.04	0.06	b.d.l.	0.05	0.04	0.11	0.07	0.06	b.d.l.	0.03
CaO	22.25	22.86	22.29	21.74	20.90	22.03	21.47	21.26	22.17	21.60	22.49	21.85	20.61	21.61	22.65	20.30
Na_2O	0.71	0.38	0.26	0.65	0.62	0.56	0.05	0.58	0.55	0.64	0.62	0.46	0.46	0.60	0.35	0.45
Total	100.45	100.20	99.65	99.56	99.29	99.37	99.31	99.00	100.10	99.02	100.03	98.83	99.03	99.23	100.66	99.57
Mg#	90.56	90.35	89.94	90.59	89.51	90.03	89.66	90.30	89.34	88.84	90.17	90.10	87.21	88.48	86.70	85.65

Mg# = Mg/(Mg+Fe); Spinel Lherz. = Spinel lherzolite; Plagio. Lherz. = Plagioclase lherzolite; Troct. Apophysis = Troctolite apophysis; Troct. Gabbro = Troctolitic gabbro

Table 4: Representative major elements plagioclase composition

	Troctolite A		Wehrlite apo.	Troctolite apo.		Troctolite B		Troc. gabbro	Troc. gabbro		Olivine gabbro		Olivine gabbro	
wt%	Core	Rim	Core	Core	Rim	Core	Rim	Core	Core	Rim	Core	Rim	Core	Rim
SiO_2	52.22	54.11	52.74	52.08	54.76	51.21	52.95	52.08	53.41	53.73	53.53	55.03	54.53	54.05
TiO_2	0.10	0.10	0.02	0.21	0.09	b.d.l.	0.06	0.30	0.10	0.07	b.d.l.	b.d.l.	0.08	0.04
Al_2O_3	30.39	29.14	30.43	30.53	28.54	30.97	29.93	30.51	29.96	29.73	29.36	28.78	29.26	29.02
Cr_2O_3	b.d.l.	b.d.l.	b.d.l.	b.d.l.	b.d.l.	0.02	0.03	b.d.l.	b.d.l.	b.d.l.	b.d.l.	b.d.l.	b.d.l.	b.d.l.
FeO	0.16	0.15	0.20	0.02	0.02	0.23	0.17	0.30	0.33	0.20	0.35	0.27	0.27	0.30
MgO	0.03	0.01	0.05	0.01	b.d.l.	b.d.l.	0.02	0.05	0.04	0.07	b.d.l.	b.d.l.	0.05	0.02
MnO	0.02	0.03	b.d.l.	0.01	b.d.l.	0.01	b.d.l.	0.02	0.07	b.d.l.	b.d.l.	b.d.l.	b.d.l.	b.d.l.
NiO	0.03	b.d.l.	0.06	b.d.l.	b.d.l.	b.d.l.	b.d.l.	b.d.l.	b.d.l.	b.d.l.	b.d.l.	b.d.l.	0.02	b.d.l.
CaO	13.35	11.25	12.78	12.79	11.17	13.14	12.15	12.71	11.84	11.39	11.14	10.93	10.90	11.02
Na_2O	3.96	5.27	4.38	4.27	5.27	3.99	4.58	4.25	4.87	5.07	5.16	5.39	5.46	5.22
K_2O	0.03	0.04	0.04	0.02	0.03	0.02	0.04	0.02	0.02	0.03	b.d.l.	b.d.l.	0.02	0.03
Total	100.28	100.11	100.70	99.93	99.88	99.59	99.93	100.25	100.64	100.29	99.54	100.40	100.59	99.70
An	65.07	54.12	61.72	62.34	53.94	64.54	59.45	62.30	57.33	55.39	54.40	52.84	52.45	53.82

An = Ca/(Ca+Na); Wehrlite apo. = Wehrlite apophysis; Troctolite apo. = Troctolite apophysis; Troct. Gabbro = Troctolitic gabbro

Table 5: Representative major elements orthopyroxene composition

	Spinel Lherz.	Plagioclase Lherzolite		Olivine Gabbro
wt%	Core	Core	Rim	Core
SiO_2	55.40	56.18	55.43	54.83
TiO_2	0.10	0.24	0.21	0.28
Al_2O_3	4.88	2.39	2.63	2.30
Cr_2O_3	0.73	0.65	0.82	0.19
FeO	6.26	6.27	5.95	10.05
MgO	32.10	32.64	31.69	30.82
MnO	0.15	0.08	0.14	0.22
NiO	0.08	0.07	0.10	b.d.l.
CaO	0.85	1.52	3.22	1.33
Na_2O	0.03	0.01	0.03	b.d.l.
Total	100.57	100.05	100.22	100.02
Mg#	90.14	90.27	90.47	84.53

Mg# = Mg/(Mg+Fe); Spinel Lherz. = Spinel lherzolite;
b.d.l. = below detection limit

Table 6: Representative major elements spinel composition

wt%	Spinel Lherz.	Dunite	Troc. A	Troct. apo.	Troc. B	Troc. Gabbro
SiO_2	b.d.l.	0.03	0.02	b.d.l.	0.05	b.d.l.
TiO_2	0.07	2.91	1.66	1.27	2.01	1.39
Al_2O_3	53.68	15.19	17.90	16.33	21.41	12.89
Cr_2O_3	14.82	38.02	35.94	38.79	35.93	42.77
Fe_2O_3	1.03	11.65	b.d.l.	b.d.l.	7.83	b.d.l.
FeO	12.78	23.60	36.35	35.93	23.20	35.89
MnO	b.d.l.	b.d.l.	0.23	0.03	b.d.l.	0.38
NiO	b.d.l.	b.d.l.	0.27	0.02	b.d.l.	0.12
MgO	18.31	8.76	6.82	7.29	8.93	6.79
CaO	b.d.l.	0.01	0.03	b.d.l.	0.01	b.d.l.
Total	100.69	100.17	99.23	99.67	99.41	100.29
Cr#	0.16	0.63	0.57	0.61	0.53	0.69
Mg#	0.70	0.31	0.25	0.27	0.34	0.25

Mg# = Mg/(Fe+Mg); Cr# = Cr/(Cr+Al+Fe^{3+}); b.d.l.= below detection limit

Table 7: Input and output melt compositions of pMELTS numerical simulations of reactive and fractional crystallization

wt%	SiO_2	TiO_2	Al_2O_3	Fe_2O_3	FeO	MnO	MgO	CaO	Na_2O	K2O	Total	Mg#	Ca#	Liquidus	ΔT_{liq}
Ini.Melt [a]	49.93	1.21	16.85	0.87	7.01	0.13	9.5	10.45	3.61	0.03	99.59	70.75	61.54	1261°C	0
5g Assim. [b]	49.5	1.16	16.05	0.85	7.11	0.13	11.4	9.95	3.44	0.03	99.62	74.08	61.51	1297°C	36
10g Assim [b]	49.11	1.1	15.32	0.84	7.21	0.12	13.12	9.50	3.28	0.03	99.63	76.43	61.55	1322°C	61
15g Assim [b]	48.75	1.05	14.65	0.83	7.3	0.12	14.7	9.09	3.14	0.03	99.66	78.21	61.53	1344°C	83
Mod.Melt [c]	52.81	1.94	15.82	0.77	5.50	0.00	8.03	10.68	4.41	0.04	100.0	72.24	57.23	1222°C	-

Mg# = Mg/(Mg+Fe); Ca# = Ca/(Ca+Na); Liquidus = Liquidus temperature; $-\Delta T_{liq} = T_{liq}$ (modif) - T_{liq} (initial)

a: Initial primitive melt composition used for fractional and reactive crystallization modeling, after Saccani *et al.* (2008).

b: Melt composition and liquidus temperature after assimilation of 5, 10 and 15 grams of olivine during 5°C cooling.

c: Melt composition modified after reactive crystallization process, used as initial melt for fractional crystallization process of the olivine gabbros.